Spring 2013

# CVD Graphene and Saturable Absorbers

Nathan Keschl
*University of Colorado Boulder*

# CVD Graphene and Saturable Absorbers

Nathan Keschl

Engineering Physics

University of Colorado at Boulder

Committee Members:

Thomas Schibli - Department of Physics

John Cumalat - Department of Physics

Scott Bunch - Department of Mechanical Engineering

*The University of Colorado*

*Boulder*

2013

# CVD Graphene and Saturable Absorbers

Nathan Keschl*
*Department of Physics, University of Colorado at Boulder, Boulder, CO 80309, USA*

(Dated: April 11, 2013)

Graphene, a single layer of carbon atoms arranged in a honeycomb lattice, has attracted attention in recent years due to its unique electronic, mechanical, and optical properties. Being one atom layer thick, it is the closest material to a two dimensional lattice. It was initially discovered by peeling scotch tape off of graphite, but since has been produced by an alternative method called Chemical Vapor Deposition (CVD). This paper explains the process, physics, and results of growing graphene via CVD.

Among many other applications, graphene has unique optical properties that occur due to its electronic band structure. These optical properties imply the potential of using graphene as a mirror to convert continuous wave lasers into pulsed lasers. This paper includes an in-depth analysis of saturable absorbers and the effectiveness of using CVD graphene for saturable absorber mirrors.

## Contents



*Electronic address: nathan.keschl@Colorado.EDU

## I. ACKNOWLEDGMENTS

I am very grateful for the unselfish support I received from numerous individuals. I would not have been able to complete this thesis without them. The courage, insight and knowledge I gained from everybody around me helped me develop not only my scientific mind but my creative mind as well. The way of scientific thinking is an art in itself. One

must be able to understand a concept so thoroughly to hypothesize about things they do not understand and develop experiments to test whether the hypothesis is correct. This involves a creative mind to be able to think outside the box to determine a solution to a problem.

Professor Thomas Schibli was my academic adviser and was very kind and patient while I learned about optics. While working the in the lab I was asked to do many tasks I was unfamiliar with, such as manufacturing a platform for a small motor, designing and soldering a circuit, aligning the laser, and working with many instruments within the lab. Thomas provided excellent guidance and support when I was struggling to learn these new skills. Chien-Chung Lee and Wanyan Xie, the graduate students in the lab, were also of great help. The depth of their knowledge and willingness to help did not go unnoticed. I would have been lost without them. Overall, I am proud have made such strong friendships with Thomas, Chien-Chung and Wanyan.

The Undergraduate Research Opportunity Program (UROP), DARPA, and the National Science Foundation provided me with financial support to perform my research. I appreciate the motivation they give undergraduates to get involved with research activities. Studying in a classroom does not offer the same experience as working a laboratory. Being able to formulate your own question and make your own mistakes taught me better than any classroom experience could. I thank UROP, DARPA, and NSF for all the support I received.

Finally, I would like to thank my family for supporting my academic and personal goals. They give me the confidence and strength to pursue things that I would never be able to do on my own. The friends I have made, inside and outside of physics, are very important to me and I would not trade them for the world. I thank each and every one of them, for they inspire me to work hard and play hard.

## II. INTRODUCTION

Graphene is a single atomic layer of carbon atoms arranged in a honeycomb lattice. The high electronic mobility and mechanical strength of graphene has captured the interest of many researchers in recent years (Geim and Novoselov, 2007; Maas *et al.*, 2008; Sun *et al.*, 2012; Ugolotti *et al.*, 2012). The near-ballistic transport at room temperature and high mobility make it attractive for high frequency applications. The electronic and mechanical

properties of graphene are ideal for transparent conducting films, electrodes, mechanical membranes, transistors, and capacitors (Sun *et al.*, 2012).

Graphene also displays ultra-fast nonlinear properties useful for ultra-short pulse generation. Due to the zero-bandgap structure and linear energy dispersion of Dirac electrons, graphene saturable absorbers can operate at a wide bandwidth. In fact, graphene saturable absorbers (GSAs) have been able to produce pulses at 1, 1.25, 1.5, and 2 $\mu$m (Sun *et al.*, 2012; Ugolotti *et al.*, 2012). GSAs boast a very fast recovery time, simple manufacturing, and a universal absorption of light ranging from ultraviolet to visible. These optical properties allow graphene to be used for saturable absorbers, polarizers, photo-detectors, optical modulators, and other electronic devices.

This paper begins with a review of CVD graphene, followed by a review of saturable absorbers and lasers. Next are the results of the CVD experiments and differential reflectivity experiments followed by an analysis of the results.

### A. My contribution to current and future research

I have made progress in the optimization of the growth parameters for CVD graphene and in the characterization of saturable absorbers at a $1.5\mu m$ center wavelength. For CVD graphene, my research has evaluated the effect that various growth parameters have on the quality and size of CVD graphene. Varying the parameters of a CVD growth and characterizing the results of each variation has allowed for larger domains of graphene and more hexagonal shaped flakes, which have advantages in many fields. Applications of graphene include transistors, capacitors and mechanical membranes. Larger area graphene allows for larger mechanical, electrical and optical devices.

Another prominent component of my research is using the graphene grown in the lab as a saturable absorber. A saturable absorber converts a continuous wave laser into a pulsed laser. For graphene saturable absorbers, I constructed a setup capable of measuring a 0.05% nonlinearity over three orders of magnitude to measure optical absorption as a function of intensity. I characterized the optical properties of graphene saturable absorber mirrors (SAMs) fabricated using various dielectrics. These results help us learn about limits of using graphene as a saturable absorber at a $1.5\mu m$ wavelength. Others may use my optical setup for measuring the differential reflectivity in other samples. Saturable absorbers are useful

for ultra-fast optical applications such as ultra-precise timing, spectroscopy, and imaging.

## III. CHEMICAL VAPOR DEPOSITION GROWTH

This section reviews the discovery of graphene and the uses of graphene, describes chemical vapor deposition growth, and concludes with the physics of graphene.

### A. Graphene 101

Sixty years ago, graphene was used as a theoretical model to describe various carbon-based materials. Twenty years ago, graphene was used as a model for (2+1)-dimensional quantum electrodynamics. However, until recently, graphene was only a theoretical model, as many people believed such a thin material would be unstable in the formation of curved structures such as the bucky ball and the nanotube (Figure 1). However, when graphene was unexpectedly found in 2004, the theoretical model became a physical material that would explode in the scientific community (Geim and Novoselov, 2007).

Graphene is a single atomic layer of carbon atoms arranged in a honeycomb lattice. It is the closest material to a 2-dimensional lattice, as a material cannot get any thinner than an atom. A drawing of graphene is shown in Figure 1 (Geim and Novoselov, 2007). This figure displays the honeycomb pattern, along with the various objects that can be made from a sheet of graphene. The shape on the left is a bucky ball, the cylinder in the middle is a carbon nanotube, and many sheets of graphene that could be stacked to make graphite on the right.

Although the first graphene was discovered by peeling scotch tape off graphite, there have been many alternative methods developed since. Some of these methods include mechanical exfoliation, liquid phase exfoliation, carbon segregation, reduction of graphene oxide, micromechanical cleavage, and chemical vapor deposition (CVD) (Sun *et al.*, 2012, 2010; Wei *et al.*, 2009). The CVD process involves flowing a hydrocarbon molecule over a metal substrate. The metal substrate will act as a catalyst to drive the decomposition of the hydrocarbon so the carbon atom can bind with the copper foil. A layer of carbon atoms will grow on the surface of the metal substrate, resulting in graphene. Mechanical exfoliation is the process of repeatedly peeling a piece of tape from graphite until just one layer of graphite

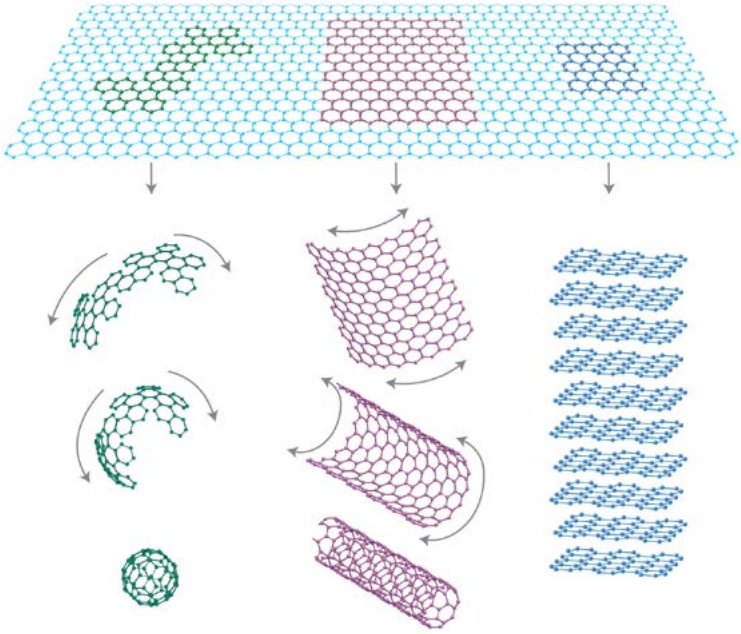

FIG. 1 A sheet of graphene (top) with patterns to construct bucky balls (left), nanotubes (middle), and multiple graphene sheets to make 3D graphite (right) (Geim and Novoselov, 2007).

(graphene) remains. Mechanically exfoliated graphene has the highest measured electron mobility. However, exfoliated graphene has limitations in the size and quantity of graphene, and is often inconsistent in the number of layers of graphite that are stripped away (Geim and Novoselov, 2007).

Large area, monolayer graphene with hexagonal domain boundaries is desirable for multiple reasons. Large area is useful because the graphene flake will be easier to find on the sample. Furthermore, a larger spot size for the laser beam can be used and the graphene flake can be better approximated as an infinite sheet when focused on the center of the flake. Larger graphene sheets also allow for larger transistors, capacitors, and other electronic devices. Hexagonal graphene is preferred because it indicates the graphene flake grew correctly, as the graphene flake should be a fractal of the smaller hexagon carbon lattice (Nagai *et al.*, 2009) (see Figure 1). Finally, monolayer graphene is best for saturable absorbers because it has broadband absorption and the best ratio of saturable to non-saturable loss. Also, there is negligible two-photon absorption whereas multilayer graphene has strong two-photon and little saturable absorption.

There are many variables that can be explored during a CVD growth, specifically the temperature. While the growths in our lab were performed at 1000°C, other groups have

shown that large area, high-quality graphene has been grown by depositing a solid carbon source, such as polymer films or small molecules, onto a metal substrate (Sun *et al.*, 2010). A group at the University of Texas at Austin varied the growth temperature of graphene, and was able to grow graphene at temperatures as cold as 600°C (Zhang *et al.*, 2012). Continuing with the low temperature growth, solid polymethyl-methacrylate (PMMA) and polystyrene precursors were used to grow monolayer graphene films at 400°C, and a benzene hydrocarbon source produced monolayer graphene at 300°C (Li *et al.*, 2011).

Copper is used as the substrate of a CVD growth. Copper is used because it does not dissolve carbon when the temperature increases, but it does lower the potential barrier for a hydrocarbon molecule to react with the copper. Therefore, carbon is able to interact with the substrate and the substrate will not dissolve the carbon. The crystallography within the copper substrate contributes to the growth parameters of graphene. Another group has determined that Cu(111) produces pristine monolayer graphene at a high growth rate while Cu(100) causes slow, multilayer graphene growth (Wood *et al.*, 2011). This proves that the substrate the graphene is grown on has an influence on the the quality and size of the graphene. In fact, A platinum foil surface was used in place of copper foil and was able to use CVD at ambient pressure to produce millimeter-sized hexagonal single-crystal graphene films (Gao *et al.*, 2012).

Theoretically, each independent variable of a growth corresponds to a dependent variable, such as the size, quality, and the number of layers. Determining how varying an independent variable affects a dependent variable helps us learn more about the physics of a growth and we use this knowledge to make the best graphene possible.

## IV. SATURABLE ABSORBERS

A saturable absorber mirror (SAM) is a mirror within a laser cavity that is used to convert a continuous wave laser into a pulsed laser. The most common type of saturable absorber today is the semiconductor saturable absorber mirror (SESAM). Lasers mode-locked by SESAMs have achieved repetition rates up to 160 GHz and pulse energies of 10J (Maas *et al.*, 2008). However, SESAMs are complex quantum well devices that are expensive, difficult to make, and have a narrow bandwidth. Graphene SAMs, conversely, only require graphene to be transferred onto a mirror, making them easy to make and inexpensive. The

band structure of graphene results in a wide bandwidth for graphene SAMs.

## A. Benefits of Graphene

Many applications of graphene arise from its attractive characteristics, including ultra-wideband absorption, controllable inter-band transition, saturable nonlinear absorption and high-mobility carrier transport (Li *et al.*, 2012). Graphene has a carrier mobility of 200,000 $cm^2/(Vs)$. Various types of optoelectronics have been fabricated using graphene. A few examples are photodetectors, polarizers, modulators and mode-locked lasers, (Li *et al.*, 2012; Liu *et al.*, 2012).

Despite only being one atom layer thick, graphene boasts a remarkable absorption of 2.3% of normal incident light ranging from ultraviolet to visible light. A universal interband-transition-induced AC conductance of $e^2/4\hbar$, where e is the charge of an electron and $\hbar$ is Planck's constant divided by $2\pi$, arises from the conical and gapless electronic band structure of graphene. For mono-layer graphene, this conductance converts to a universal absorption coefficient of $e^2/4\epsilon_0\hbar c = 2.3\%$, where $\epsilon_o$ is the permittivity of space and c is the speed of light (Li *et al.*, 2012; Liu *et al.*, 2012).

## B. Physics of Graphene

### 1. Conductors, Semiconductors and Insulators

Another reason science has been so attracted to graphene is due to its electronic band structure. The electronic band structure of a material is characterized by its electron transport behavior. The three main types of materials, defined by their band structure, are conductors, semiconductors and insulators (Figure 2). An insulator will have a large bandgap between the valence band and the conduction band. This large bandgap results in a large amount of energy needed to excite an electron from the valence band into the conduction band, which generally does not happen at room temperature. The opposite of an insulator is a conductor. Within a conductor, the fermi level (the level at which electrons are filled to) is within the conduction band and therefore electrons in a conductor can move freely. Finally, a semiconductor is between a conductor and an insulator, with a small bandgap so electrons can be excited into the conduction band at non-zero temperature.

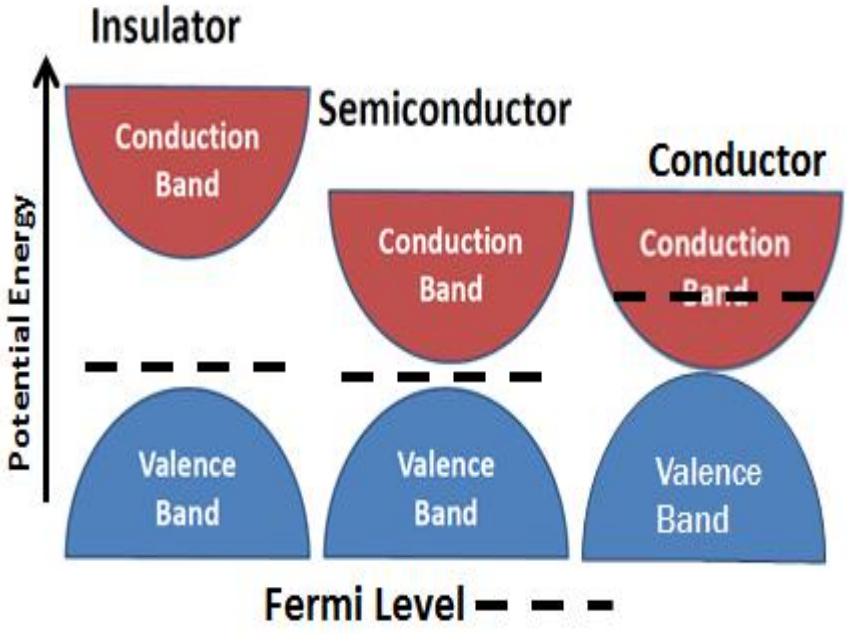


FIG. 2 Band structures for insulators, semiconductors and conductors. The valence band is on bottom and the conduction band is on top. An insulator has a large band gap, requiring more energy to excite an electron from the valence band to the conduction band. A conductor has electrons in the conduction band which can flow freely. A semiconductor has a small band gap where electrons can be excited to the conduction band.

The ability to excite electrons from the valence band into the conduction band can be summarized by the Boltzmann distribution law, which states that at thermal equilibrium, the probability of an electron occupying a particular state is proportional to

$$Prob \ \alpha \ e^{-\epsilon/kT} \tag{1}$$

where $\epsilon$ is the energy of the state, T is the temperature and k is the Boltzmann constant (Widom, 2002).

Therefore, as the bandgap increases, the probability for an electron to be excited into the conduction band decreases exponentially. At room temperature, this probability is very small for an insulator (the bandgap is typically a few eV) but not so small for a typical semiconductor (for example, silicon has a bandgap of 1.1eV). For graphene, due to its vanishing bandgap, there are always some thermal-excited electrons in the conduction band at room temperature.

## 2. Band Structure of Graphene

Graphene's electronic band structure is displayed in Figure 3 (Castro Neto *et al.*, 2009), with the valence band on bottom and the conduction band on top. The right part of the image shows the band structure at a Dirac point. Notice the point-like bandgap and the linear relation between the energy (E) and momentum (k) in the x and y directions, related by a constant c=2.7eV ($E = \pm ck$).

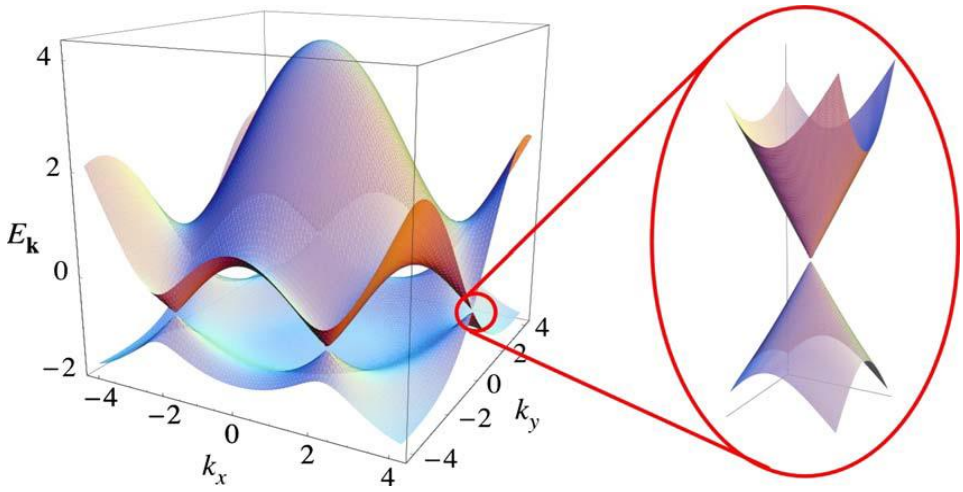


FIG. 3 The electronic band structure of graphene in momentum space. On the right is a zoomed in portion of the crystal lattice, displaying the point-bandgap structure and linear energy dispersion of Dirac electrons. The conduction band is on top while the valence band is on bottom.

When no light is shined on the graphene at room temperature, the valence band is full of electrons and the conduction band is empty (except for a few thermally excited electrons). Initially, a photon of energy $\hbar\omega$, where $\omega$ is the frequency of the photon, is absorbed by the graphene, promoting an electron from the valence band into the conduction band as shown Figure 4A. Due to electron-electron and electron-phonon cooling, the electron then relaxes down to a lower energy level (Figure 4B). The unique property of the zero-band gap results in a quicker relaxation time of the electron from the conduction band to the valence band. For other semi-conductors with a band gap, a photon would be need to be emitted for the electron to fall back into the valence band, resulting in a longer relaxation time. Graphene does not have a band gap, therefore the electrons can fully relax down to the valence band without emitting a photon. Finally, as the intensity of incoming photons increases, the number of electrons promoted to the conduction band also increases. Eventually, when the

intensity of incoming light reaches the saturation intensity, there will be a hole in the valence band so an incoming photon will, on average, be transmitted, shown in Figure 4C. Therefore, graphene strongly absorbs lower intensities of light and weakly absorbs higher intensities.

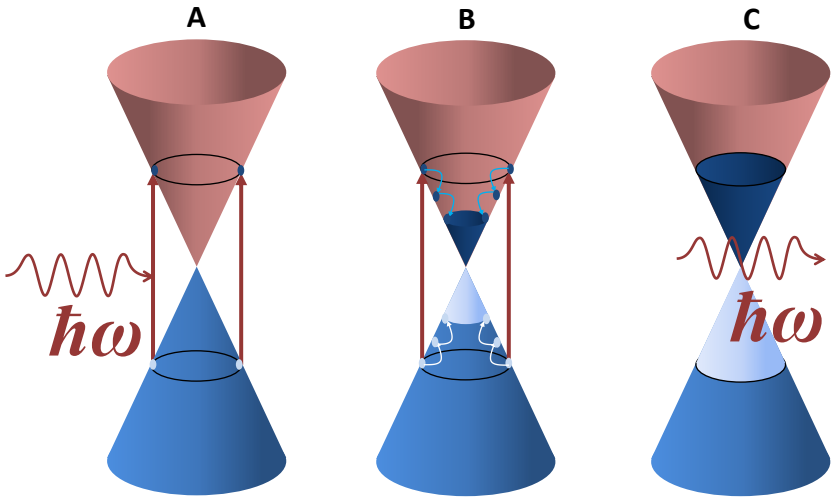


FIG. 4 This figure displays the electronic band structure of the crystal lattice within graphene. The conduction band is shown on the top while the valence band is on the bottom. The lattice begins with no light shined, so all the electrons are in the valence band on bottom. Then, a photon of energy $\hbar\omega$ is absorbed by the crystal lattice, exciting an electron to the conduction band (A). This electron will then relax down to a lower energy level due to electron-electron and electron-phonon scattering (B). Finally, if the intensity of incoming photons is great enough so there is a hole in the valence band, an incoming photon will, on average, be transmitted (C) (Lee *et al.*, 2012b).

### 3. Fast Recovery Time

A saturable absorber is characterized by its relaxation time. The faster the relaxation time, the shorter the pulse. Simulations show that when excited carriers are stimulated by electron-phonon scattering, a population inversion can be achieved at energies determined by the photon energy. However, when electron-electron scattering is introduced, the carrier energy distributions are quickly thermalized, resulting in a fast relaxation of photoexcited carriers (Kim *et al.*, 2011). The relaxation time of graphene is on the time scale of $<100fs$ for the intraband carrier-carrier scattering, and the time scale of 1.5ps for optical phonon

cooling and interband carrier recombination (Ugolotti *et al.*, 2012), as can be seen in Figure 5.

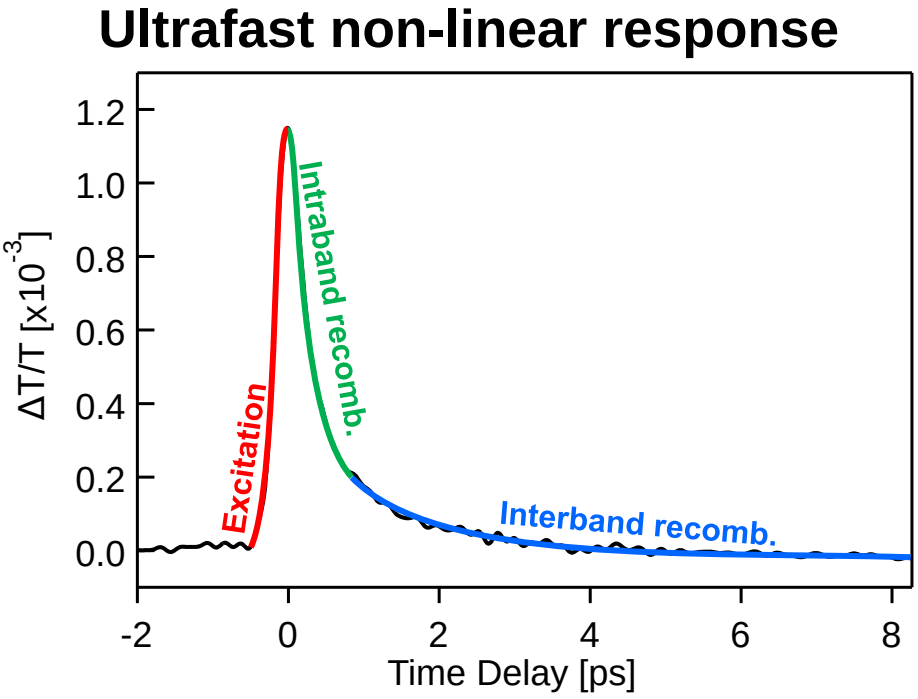


FIG. 5 The relaxation time of graphene. The intraband recombination happens in $<100fs$ and the interband recombination happens in $\sim 1.5ps$ (Lee *et al.*, 2012a)

### C. Saturable Absorber

A saturable absorber mirror (SAM) is a mirror that strongly absorbs low intensity light and weakly absorbs high intensity light. Figure 6 shows a plot of percent reflectivity as a function of intensity. The percent reflectivity is on a linear scale while the intensity is on a logarithmic scale. The characteristic parameters of a saturable absorber are the saturable loss, the non-saturable loss, the damage intensity, and the saturation fluence. The non-saturable loss is the loss that occurs at all intensities as a result of merely inserting the saturable absorber. A zero non-saturable loss is desired to minimize the loss of the laser cavity. The saturable loss is the difference between the loss when the saturable absorber is not saturated and when it is fully saturated. The insertion loss is defined as the total loss at low intensities (saturable + non-saturable). Finally, the saturation fluence is the point at which the SAM will become saturated and begin to reflect more of the high intensity light.

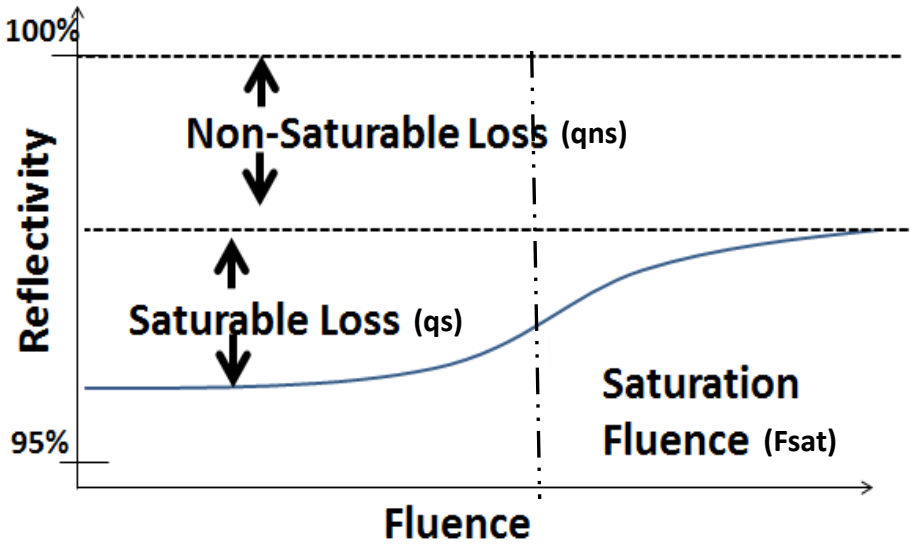


FIG. 6 This figure displays the reflectivity of a saturable absorber as a function of pulse fluence. The non-saturable loss (qns) is the loss that occurs at all intensities, as a result of merely inserting the saturable absorber. The saturable loss (qs) is the loss caused by the saturable absorber as it becomes saturated. The saturation fluence (Fsat) is the point at which the SAM will begin to reflect more of the high intensity light.

This is useful for converting continuous lasers into pulsed lasers because as a pulse of light passes through the absorber, the absorber will strongly absorb the low intensity wings of the pulse and weakly absorb the high intensity peak of the pulse. This absorption will shorten the pulse (Figure 7). After several iterations of passing through a saturable absorber, the pulse becomes shorter and shorter until the dispersion and bandwidth of the laser limit the pulse width. In order to get a short pulse of light, a superposition of many frequencies of light is required. However, a laser only lases in a certain range of frequencies that can be superimposed, limiting the shortness of the pulse.

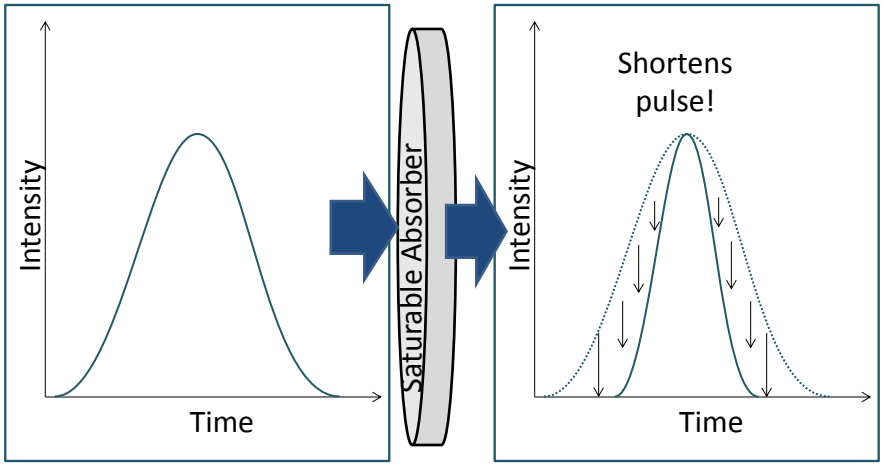


FIG. 7 This figure displays a Gaussian pulse passing through a saturable absorber. As the pulse pass through, the lower intensity 'wings' of the pulse are strongly absorbed while the high intensity peak is weakly absorbed, resulting in a shorter pulse.

### 1. Fabrication of Satuable Absorber Mirrors

To use graphene as a saturable absorber, it must first be transferred from the copper foil it was grown on onto a mirror. After over-growing CVD graphene (such that the flakes grow into each other), the graphene is spin-coated with polymethyl-methacrylate (PMMA). The copper foil is then etched away with $Fe_2Cl_3$ or $Fe(NO_3)_3$ in $H_2O$. Finally, the graphene layer is transferred onto a substrate, the PMMA is dissolved with acetone, and only the graphene and substrate remain. This process is depicted in Figure 8.

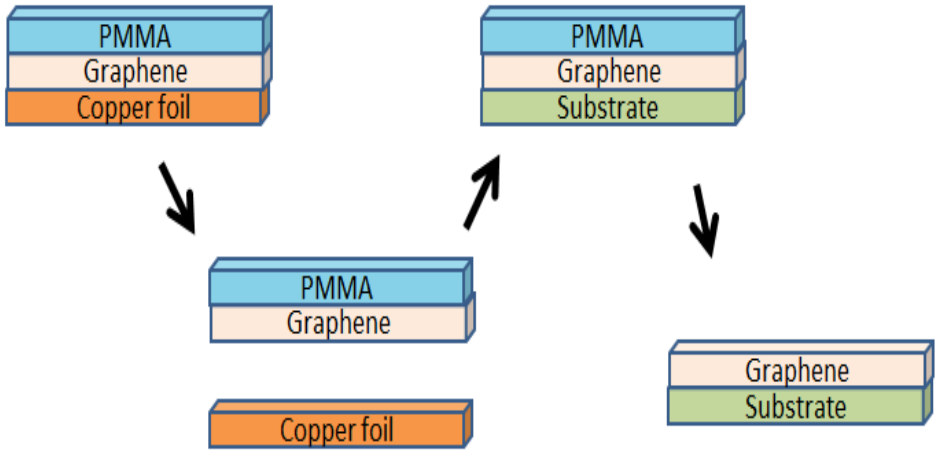


FIG. 8 The transfer process of graphene on a copper foil onto a substrate. First, the graphene is spin-coated with PMMA. The copper is then etched away with $Fe_2Cl_3$ or $Fe(NO_3)_3$ in $H_2O$. Then the graphene is transferred onto a substrate and the PMMA is dissolved with acetone.

Various substrates were used to investigate how the graphene reacted with each substrate. A graphene SAM can be constructed using one of two configurations. In one configuration, called bottom-coated graphene, one side of the graphene is bonded to a dielectric while the other side is exposed to air, as can be seen in Figure 9 on the left. The other configuration displayed on the right, called top-coated graphene, consists of the graphene being sandwiched between the glass slide and a dielectric.

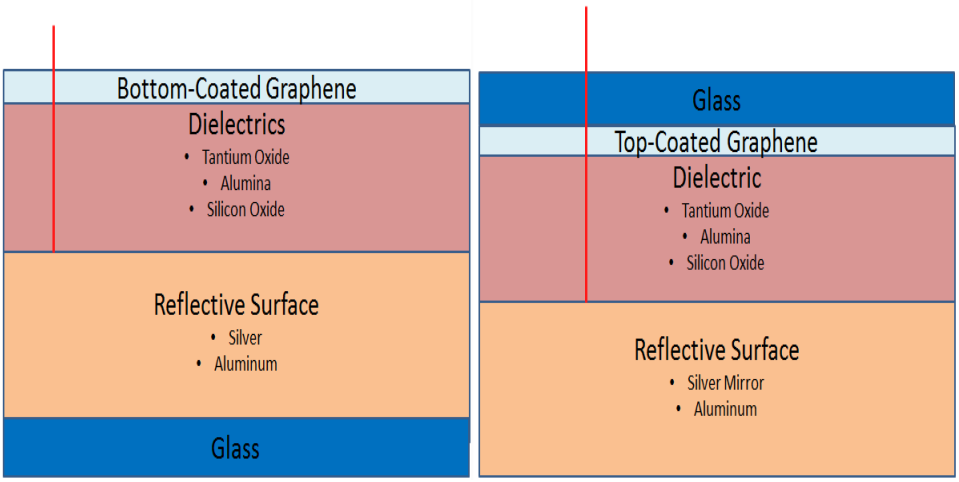


FIG. 9 Top and bottom coated graphene saturable absorbers. On the left is bottom-coated graphene. A reflective surface of either silver or aluminum is deposited onto a glass slide. Then, a dielectric (ether Tantium Oxide, Alumina, or Silicon Oxide) is deposited onto the reflective surface and finally the graphene on top of the dielectric. The top-coated graphene (right) first deposits graphene onto the glass slide, then the dielectric and reflective surface.

Various substrates and configurations of graphene SAMs lead to different optical properties of the SAM. The thickness of the dielectric affects the field-enhancement of the electric field at the location of the graphene. Figure 10 shows the normalized field intensity as a function of position from the mirror (Lee *et al.*, 2012b).

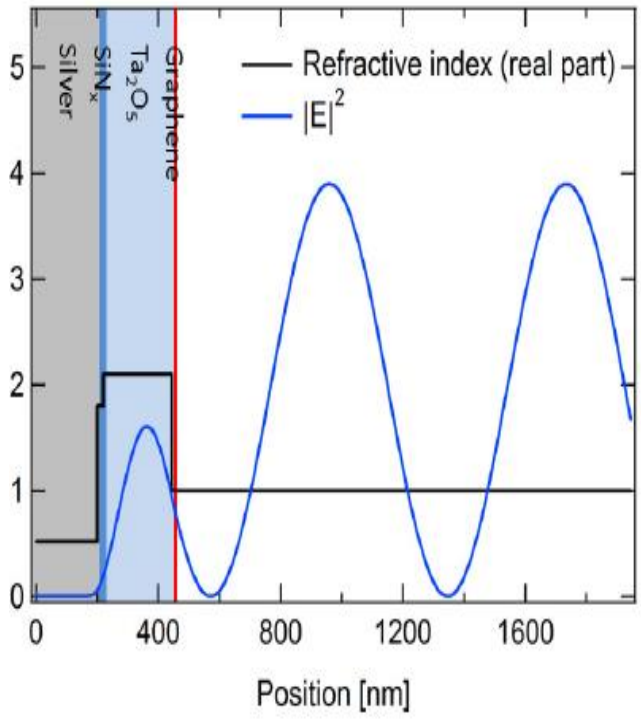


FIG. 10 The field enhancement of graphene as a plotted as a function of position from mirror. (Lee *et al.*, 2012b)

### 2. Fit Equation for Satuable Absorbers

The saturation of an absorber can be modeled by the equation (Carmichael *et al.*, 2004):

$$\frac{dq(t)}{dt} = -\frac{q(t) - q_o}{T_{recovery}} - \frac{q(t)P(t)}{E_{sat}} \tag{2}$$

where $q_0$ is the saturable loss, q(t) is the loss coefficient at time t, P is the power, and $E_{sat}$ is the absorber saturation energy.

At any time t, the reflected intensity $I_{out}(t)$ of a saturable absorber is:

$$I_{out(t)} = R(t)I_{in}(t) = e^{-2q(t)}I_{in}(t) \tag{3}$$

where R is the reflectivity.

The total net reflectivity is therefore

$$R_{tot} = \int \frac{I_{out}(t)dt}{I_{in}(t)dt} = \frac{F_{out}}{F_{in}} = 1 - \frac{2}{F_in}\int q(t)I_{in}(t)dt = e^{-2q_p} \tilde{=} 1 - 2q_p \tag{4}$$

where F is the fluence and $q_p$ is the total absorber loss coefficient.

Then, from equations (3) and (4) it follows:

$$q_p = \frac{1}{F_{in}} \int q(t) I_{in}(t) dt = \int q(t) f(t) dt \tag{5}$$

where

$$f(t) = \frac{I_{in}(t)}{F_{in}} = \frac{P_{in}(t)}{E_{p,in}} \;\; with \;\; \int f(t) dt = 1 \tag{6}$$

To model the graphene saturable absorber as a fast saturable absorber, the absorber recovery time must be much faster than the pulse duration ($T_{pulse} >> T_{recovery}$). The slow saturable absorber is just the opposite ($T_{pulse} << T_{recovery}$). With $T_{pulse} = 250fs$ and $T_{recovery} = 100fs$, the graphene saturable absorber lies somewhere in between.

*a.* Slow Saturable Absorber

For a slow saturable absorber ($T_{pulse} << T_{recovery}$), we can ignore the recovery of the absorber during pulse excitation and equation 2 can be approximated as

$$\frac{dq(t)}{dt} \tilde{=} - \frac{q(t) P(t)}{E_{sat}} \tag{7}$$

which has the solution

$$q(t) = q_0 \, exp[-\frac{E_p}{E_{sat,A}} \int f(t') dt'] \tag{8}$$

then, when q(t) is plugged into equation 5, the total absorber loss coefficient can be solved for as a function of pulse fluence $F_{p,A}$

$$q_p(F_{p,A}) = \int q(t) f(t) dt = q_0 \frac{F_{sat,A}}{F_{p,A}} (1 - exp[-\frac{F_{p,A}}{F_{sat,A}}]) \tag{9}$$

which is the fit equation used for a slow saturable absorber.

*b.* Fast Saturable Absorber

Conversely, for a fast saturable absorber, the pulse duration is much longer than the recovery time ($T_{pulse} >> T_{recovery}$), and equation 2 reduces to

$$0 = -\frac{q(t) - q_o}{T_{recovery}} - \frac{q(t)P(t)}{E_{sat}} \tag{10}$$

which has the solution

$$q(t) = \frac{q_0}{1 + \frac{I_A(t)}{I_{sat,A}}} \tag{11}$$

(using the fact that $P_{sat,A} = E_{sat,A}/T_A$ and $P(t)/P_{sat,A} = I_A(t)/I_{sat,A}$)

Finally, substituting equation 11 into equation 5, the total absorber loss coefficient as a function of pulse fluence is

$$q_p(F_{p,A}) = \frac{1}{F_{p,A}} \int q(t)\ I_A(t)\ dt = q_0\ (1 - \frac{1}{3}\frac{F_{p,A}}{T\ I_{sat,A}}) \tag{12}$$

which is the fit equation used for a fast saturable absorber.

Because graphene is between a fast and slow absorber, we take the average of the fast and slow equations (equations 9 and 12).

The average of a fast and slow absorber is:

$$q_p(F_{p,A}) = \frac{q_0\ (1 - \frac{1}{3}\frac{F_{p,A}}{T\ I_{sat,A}}) + q_0\frac{F_{sat,A}}{F_{p,A}}(1 - exp[-\frac{F_{p,A}}{F_{sat,A}}])}{2} \tag{13}$$

Figure 11 shows the fits of equations 9 (slow), 12 (fast), and 13 (average).

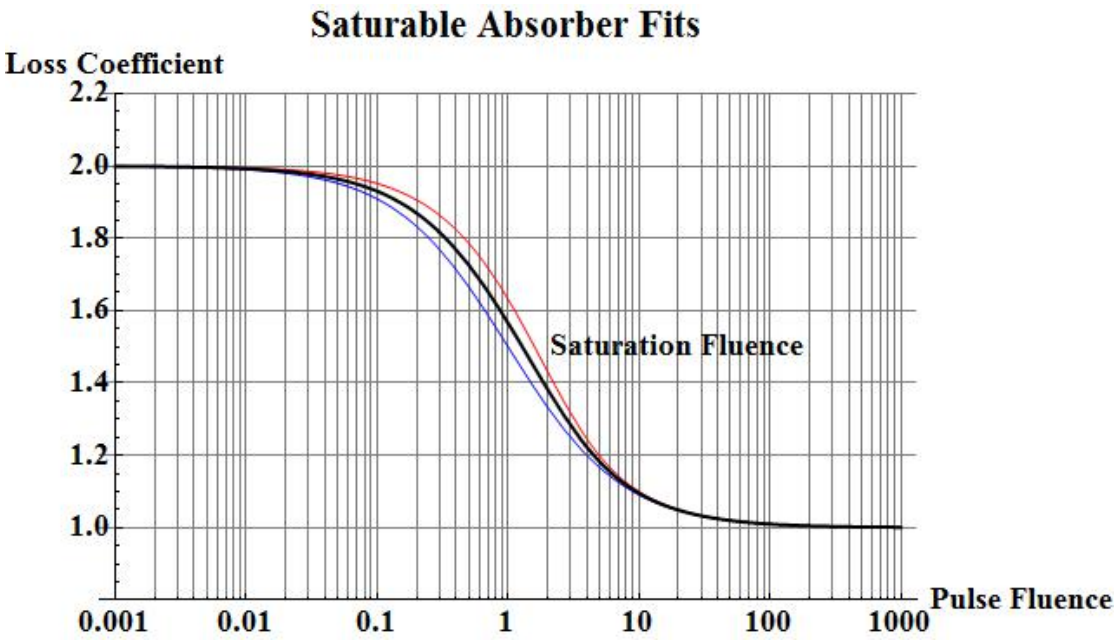


FIG. 11 Here, the fit equations of slow (eq. 9), fast (eq. 12), and the average of slow and fast saturable absorbers (eq. 13) are displayed. The fast absorber is blue, the slow absorber is red, and the average of the fast and slow is black. The saturation fluence, saturable loss, non-saturable loss were all equal to one to demonstrate each fit equation.

Some experiments performed on the saturable absorbers measured the reflection coefficient (Figure 6), which is 1 - the loss coefficient.

## V. LASERS

This section describes the physics of lasers, including stimulated emission and mode-locking.

Lasers, an acronym for Light Amplification by Stimulated Emission of Radiation, have been one of the most powerful scientific tools since its discovery. To understand how a laser works, one must first understand the concept of stimulated emission. The fundamental idea of stimulated emission begins with quantum mechanics: the energy levels of a bound system are broken up into discrete intervals. The simplest model is the two level system, as depicted in Figure 12. Imagine an electron in the ground state of an atom (Figure 12A). This atom may absorb a photon, which will excite the electron into a higher energy level, but only if the photon carries the exact amount of energy required ($E_{excited} - E_{ground}$) (Figure 12B).

Therefore, this photon has a frequency $\nu$ of $\nu = (E_{excited} - E_{ground})/h$, where h is Planck's constant and $E_{excited}$ and $E_{ground}$ are the energy levels of the ground and excited states. Depending on the stability of the energy level, the electron will stay excited for a certain amount of time before it spontaneously relaxes. Before the electron relaxes to the ground state through spontaneous emission, if another photon of the same frequency interacts with the atom, the photon will stimulate the atom, causing the excited electron to relax down to the ground state. When the electron relaxes to the ground state, the atom will emit a photon of the same phase and energy of the stimulating photon (Figure 12C). This doubling of the photons results in a power gain of the light, which is the core principle of a laser.

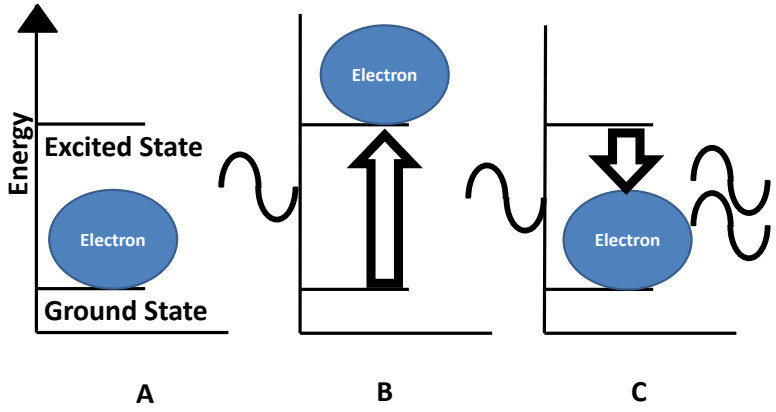


FIG. 12 This figure shows a two level system. The electron begins in the ground state of the atom (A), the atom absorbs an incoming photon and excites the electron to an excited state (B). Another incoming photon interacts with the atom and stimulates the electron to relax down to the ground state. As the electron relaxes, it emits a photon of the same energy and phase as the incoming photon, producing gain (C).

However, an actual laser works on a multi-level system because a population inversion is required for gain. A population inversion refers to the situation where the higher energy levels are more populated with electrons than the lower energy levels. This is required for gain because when the electrons are in the lower energy states, the atoms will favor absorption of an incoming photon. However, if there is a population inversion, the atoms will favor stimulated emission, resulting in gain. With the aforementioned two-level system, a population inversion is impossible because only half of the electrons can be pumped up to the excited state. If half of the electrons have already been pumped to the excited state,

further pumping will result in an equal amount of stimulated emission and absorption, and the material will then be transparent. This process is often referred to as two-level saturation (Svelto, 1989, Principles of Lasers Third Edition).

A multi-level system, on the contrary, is able to create a population inversion. For a continuous wave laser, a four-level system is required (Figure 13). According to Boltzmann statistics, essentially all atoms are initially in the ground state at room temperature. Now, as the electrons are pumped from the ground state to the third excited state, the electrons will quickly ($\sim$ ns) decay down into the second excited state because the third excited state is unstable. Therefore, the third excited state is approximately empty as it is constantly gaining and immediately losing electrons. The second excited state, which is more stable ($\sim$ms), then begins to fill. This creates a population inversion between the first and second excited states. Here, the first electrons will spontaneously relax down to the first excited state, emitting a photon with energy $E_2 - E_1$. When this photon is reflected back at the atom, it will stimulate more electrons in the second excited state to relax down, emitting addition photons of the same phase and energy. This multiplying of photons is called gain. When the electrons relax down to the first excited state by stimulated emission, a fast decay to the ground state allows the electrons to be pumped to the third excited state again. The first excited state should be at a high enough energy such that thermally excited electrons do not occupy this state.

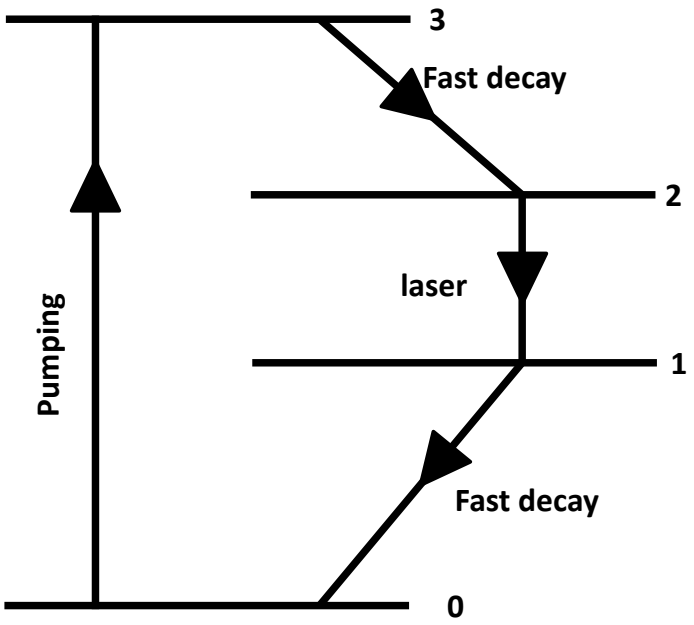


FIG. 13 This depicts a four-level laser. Electrons are initially pumped from the zero energy level to the third energy level. Electrons then quickly decay to the second energy level. Here, a population inversion can occur between levels 2 and 1. The stimulated emission forces the electrons to relax down to the first energy level. Finally, the electrons quickly decay from the first excited state to the ground state (Svelto, 1989, Principles of Lasers Third Edition).

Figure 14 shows a laser. The gain medium is placed in the center of the laser cavity and contains the multilevel atoms which will amplify the laser light. One mirror is a saturable absorber mirror, which will convert the continuous laser light into pulsed laser light. The other mirror is an output coupler, which transmits a small percentage of the laser light. As the pulse travels back and forth within the laser cavity, a small percentage of the light is transmitted every time the pulse is reflected off the output coupler. This transmitted light has a well defined direction because any light that is not in the laser path will bounce out of the laser cavity. Therefore, the length of the laser cavity determines the repetition rate of the laser. The pulse travels at the speed of light, therefore the repetition rate is c/2L, where L is the length of the laser cavity.

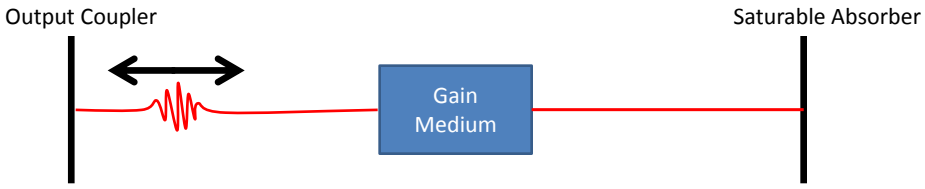


FIG. 14 This is a cartoon of a laser cavity. The gain medium amplifys the laser light. The saturable absorber converts the laser light into a pulse, and the output coupler will transmit a small percentage of the laser light.

### A. Mode-Locking

Mode-locking refers to a technique for generating ultrashort (picosecond-femtosecond) pulses from a laser. The many modes within the laser cavity are made to oscillate with comparable amplitudes and locked phases. The modes within the laser cavity are defined by the laser cavity and they have frequencies of $f = n\frac{c}{2L}$, where n is an integer number and L is the length of the cavity.

Now suppose there are 2n+1 longitudinal modes oscillating with the same amplitude $E_o$. If these modes are locked together, the phase of the $l$ mode, $\phi_l$, will be related to the phase of the $l-1$ mode $\phi_{l-1}$ mode by a constant $\phi$ (Svelto, 1989, Principles of Lasers Third Edition).

$$\phi_l - \phi_{l-1} = \phi \tag{14}$$

The total electric field E(t) at a given point in the output beam can be written as

$$E(t) = \sum_{-n}^{n} E_o exp(i[(\omega_o - l\Delta\omega)t + l\phi]) \tag{15}$$

where $\omega_o$ is the center frequency and $\Delta\omega$ is the frequency difference between consecutive modes. At the point where the phase of the center mode is zero, equation 15 simplifies to

$$E(t) = A(t)exp(i\omega_o t) \tag{16}$$

where

$$A(t) = \sum_{-n}^{n} E_o exp(il[\Delta\omega t + \phi]) \tag{17}$$

Then, at a time such that $\Delta\omega t' = \Delta\omega t + \phi$, equation 17 becomes

$$A(t') = \sum_{-n}^{n} E_o exp(il[\Delta\omega t']) \tag{18}$$

The sum on the right side of the equation is a geometric progression with a ratio equal to $exp(i\Delta\omega t')$ and A(t') is calculated to give

$$A(t') = E_o \frac{sin[(2n+1)\Delta\omega t'/2]}{sin[\Delta\omega t'/2]} \tag{19}$$

The intensity is proportional to $A^2(t')$ and when intensity is plotted against t' (Svelto, 1989, Principles of Lasers Third Edition), a curve similar to the one on the bottom left of Figure 15 is generated. On the left of Figure 15, the phases of five frequencies of light within the laser cavity are locked together. These frequencies interfere to create a short pulse of light. On the right, the phases of the frequencies are slightly out of phase, resulting in a wider pulse. Mode-locking can be done by introducing a loss element in the cavity. Its optical loss can either be modulated by an external electric signal (active) or be modulated according to the intensity of the light in the cavity (passive). Ultrashort ($<1ps$) pulses are generated mainly by mode-locking, which will be the focus of the following discussion. Passive mode-locking uses a saturable absorber that will strongly absorb low intensity light and weakly absorb high intensity light.

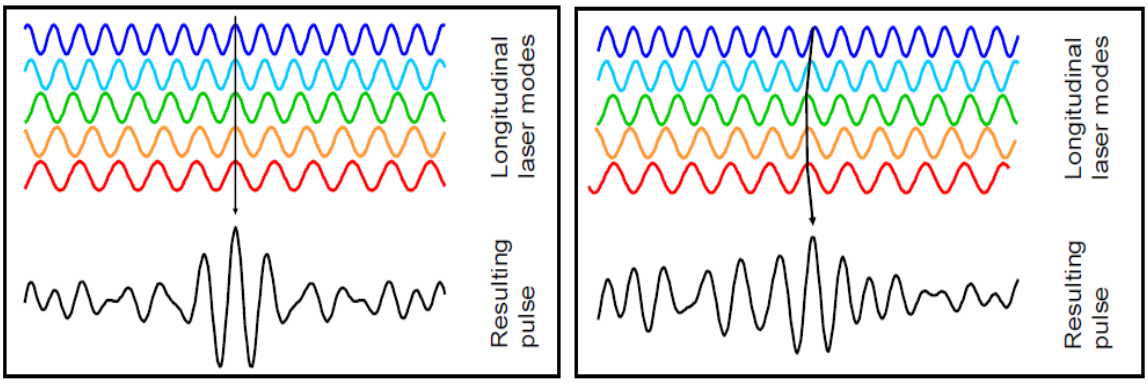


FIG. 15 On the left, the phases of many frequencies of light within the laser cavity are locked together. These frequencies interfere to create a short pulse of light. On the right, the phases of the frequencies are slightly out of phase, resulting in a wider pulse (Figure from Thomas Schibli).

Another interesting feature that arises from Figure 15 is the superposition of many frequencies of light. A very short pulse requires an infinite number of frequencies of light to be superimposed. However, a laser has a finite bandwidth, and therefore the shortness of the laser pulse is limited.

## VI. EXPERIMENTS

### A. CVD Growth

There are many parameters that can be varied in a CVD growth of graphene. These parameters include the type of metal used for the metal foil, the temperature of the growth, the time of growth, the time of annealing, the precursor gases used, the gases used in the growth, the flow rates of the gases, and the pressure and partial pressures of the growth. This section analyzes the results obtained from varying the parameters of growth to improve recipes for the future.

With CVD, experiments were performed with Torr-level pressure during the growth of graphene. Higher pressure during the growth phase will favor hexagon graphene shapes over the undesired flower shapes that occur at lower pressures. An example of hexagon-shaped graphene is displayed in Figure 16 while more flower shaped graphene is in Figure 17. Hexagonal graphene is preferred because it indicates the graphene flake grew correctly, because the graphene flake should be a fractal of the smaller hexagon carbon lattice (Nagai *et al.*, 2009) (see Figure 1).

FIG. 16 An optical microscope image of a hexagon shaped flake of graphene on a copper foil. Scale bar is 5 microns.

FIG. 17 An optical microscope image of a flower shaped flake of graphene on a copper foil. Scale bar is 5 microns.

### 1. CVD Equipment Set-up

The CVD growth set-up consists of a vacuum pump, a furnace, gas tanks and a computer (Figure 18). The graphene is grown on a copper foil that is located inside a glass tube inside of the furnace. The furnace is operated at $1000^{o}$C for the entire growth. The gas tanks are attached to one end of the glass tube and mass flow controllers are used to control the flow rates of each gas. A vacuum pump is attached to the other end of the tube and operates in the milliTorr to Torr regime when gas is flowing. The mass flow controllers, the furnace and the vacuum pump are all controlled by a computer.

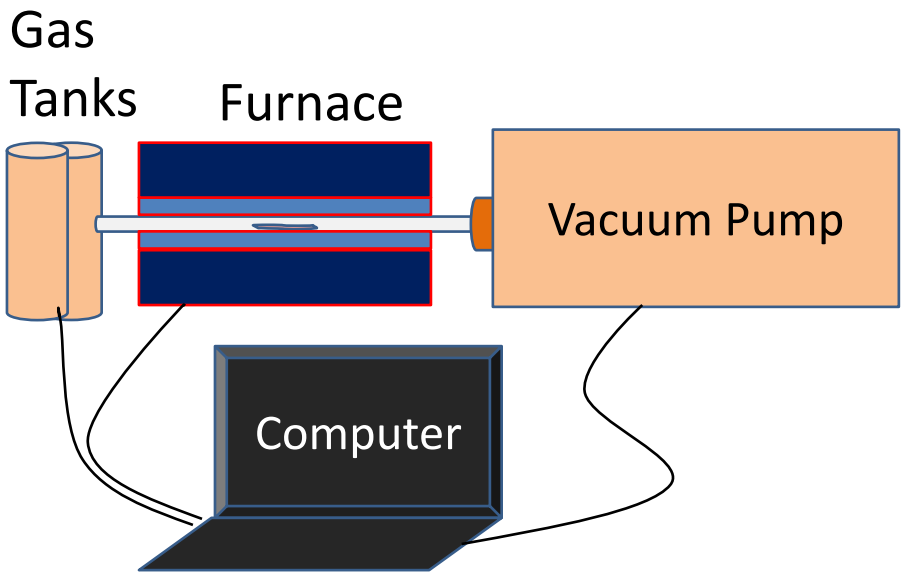


FIG. 18 Cartoon of the CVD setup. Ar, $H_2$, and $CH_4$ gas tanks are on the left, the furnace in the middle, and the vacuum pump is on the right. The copper foil is placed inside the glass tube inside the furnace.


FIG. 19 An image of the actual setup, with the furnace on the left and the vacuum pump on the right.

The copper foil inside the tube acts as a catalyst that carbon will react with to form graphene. Hydrogen is used to control the partial pressure of hydrogen to methane while argon is used to control the total pressure. Figure 20 shows methane reacting with the copper foil while argon and hydrogen pass through the tube.

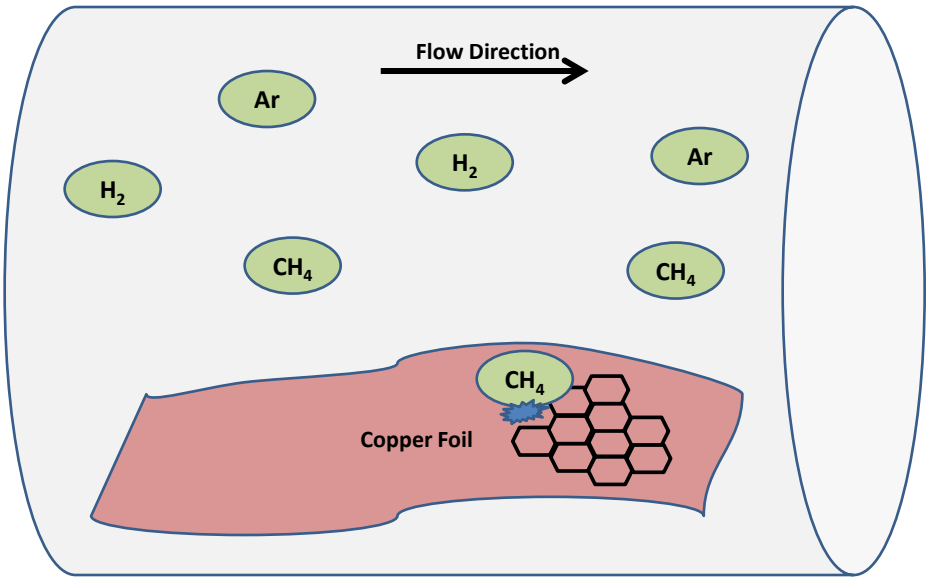


FIG. 20 This is a model of Ar, $H_2$, and $CH_4$ molecules flowing over the copper foil within the glass tube in the furnace. The $CH_4$ molecules will deposit carbon onto the copper foil, forming graphene.

The copper foil is machine pressed, 0.025 mm thick, 99.8 percent copper. Figure 21 shows the long machining marks of a piece of copper, which indicates the copper foil is not perfectly flat. To account for these machining marks and other imperfections on the copper, the copper is baked at 1000$^o$C at low pressure (few milliTorr) for half an hour. This low pressure evaporates the copper on the surface of the foil, resulting in a smoother surface.

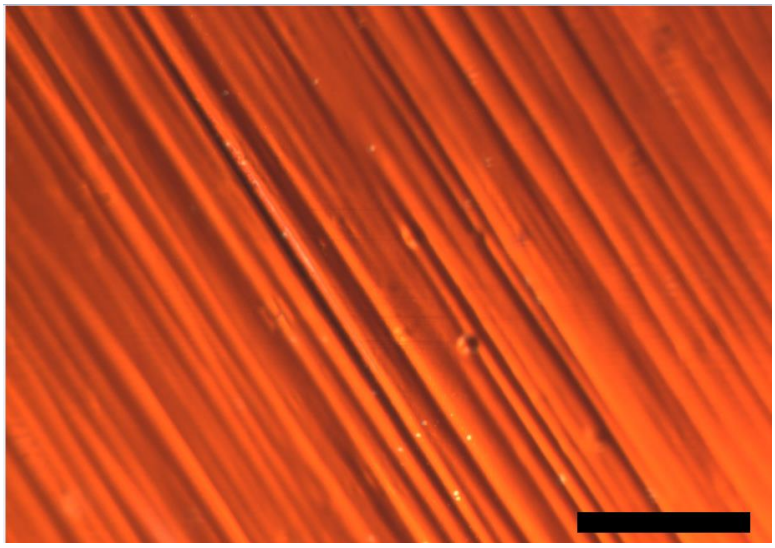

FIG. 21 An optical microscope image of machining marks present of the copper foil. Scale bar = 80 $\mu$m.

When growths were performed at this low pressure, the size of the flakes were limited to about ten microns. This size limit is due to the evaporation of copper at low pressure. At low pressures, the copper evaporates. If methane is flowed at this low pressure, the methane reacts with the copper to form graphene. The graphene then acts as a shield, preventing any copper beneath it from evaporating away. However, the copper still evaporates away from the areas surrounding the graphene. The graphene will continue to grow on the copper until the angle between the graphene and the copper is too great, therefore limiting the size of the graphene (Figure 22).

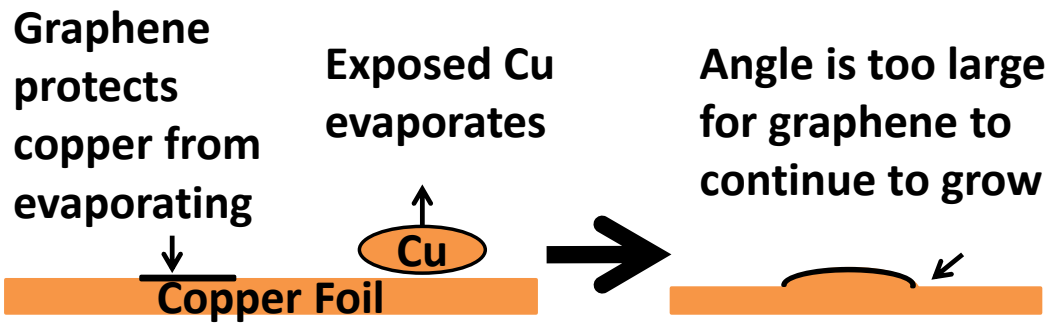


FIG. 22 A sketch depicting copper evaporating. On the left, a flake of graphene (black) has begun to grow. The graphene shields the copper beneath it from evaporating, but the exposed copper will continue to evaporate. On the right, more copper has evaporated, and the graphene has grown some to compensate for the curvature. However, the angle is now too large that the graphene cannot grow more, limiting its size.

To accommodate for the copper evaporation, higher pressure growths were performed. At higher pressures, less copper evaporates, and therefore the graphene can grow to a larger size. However, at higher pressures, more seeds will form. A seed is the first copper atom that reacts with the copper foil, seeding the beginning of a new copper flake. A low pressures, fewer seeds occur because the pressure force on the methane molecules is small. At higher pressures, the force is larger and more seeds form. When more flakes form, they can become too dense and will grow into surrounding flakes before the flakes can grow larger. Finding the right pressure where the copper will not evaporate and the density is not too high is essential.

When graphene flakes grow together, they are not as perfect as a single, continuous flake. Other groups have performed measurements on graphene boundaries, and show that grain boundaries alter the electrical properties of graphene and severely weaken the mechanical strength of graphene membranes (Huang *et al.*, 2011). Graphene not at a grain boundary is displayed in Figure 23A while a grain boundary is displayed in Figure 23B.

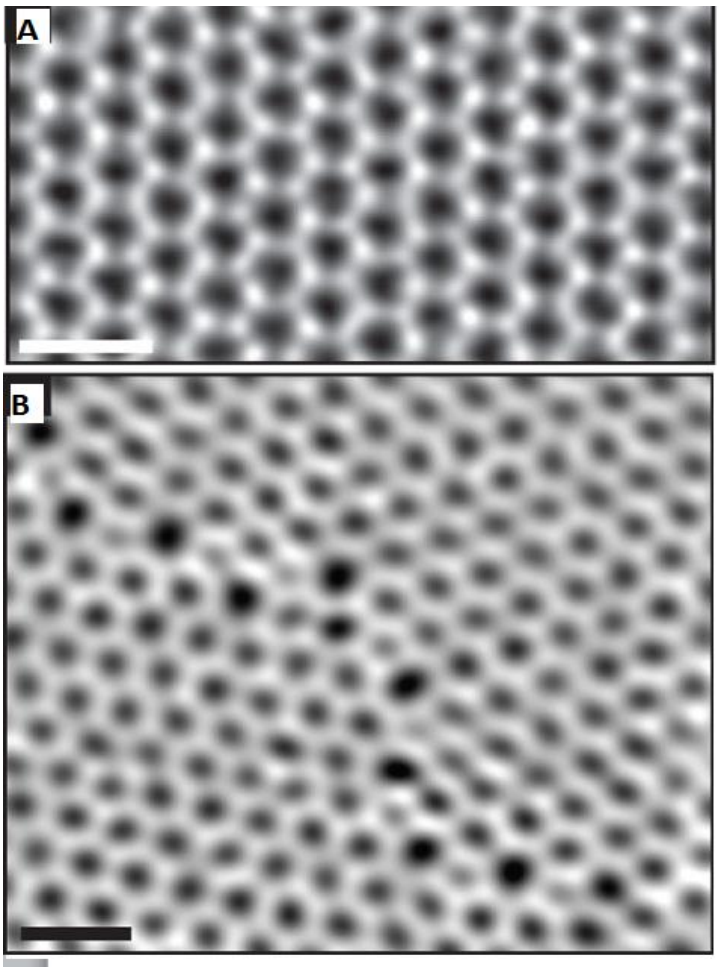


FIG. 23 This is scanning electron microscope image of graphene not at a grain boundary (A) and graphene at a grain boundary (B). The scale bars are 5$\mu$m. (Huang *et al.*, 2011)

### 3. Recipe Effects

The first parameter tested is the time for each stage of the growth. In every growth, there was an hour and 20 minutes needed for the furnace to heat up, 30 minutes to anneal the copper foil, and three hours for the furnace to cool down after the growth. The growth stage, after the annealing stage, was varied from ten minutes to four hours.

Figure 24 shows three growths, all with 5 standard cubic centimeters per minute (SCCM) hydrogen and 10 SCCM methane. Figure 24A has a growth time of 10 minutes, Figure 24B has a growth time of 30 minutes, and Figure 24C has a growth time of 50 minutes. The length scale in the figure is 50 microns. This figure shows the size of the graphene flakes as a function of time. However, longer times resulted in the graphene flakes growing together,

which made it impossible to measure the size of a flake. Less dense samples were needed.

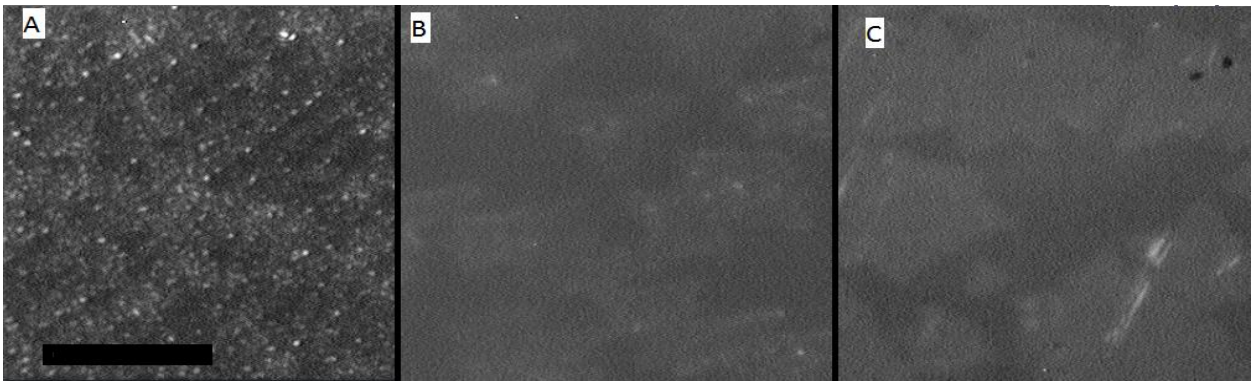


FIG. 24 Optical microscope image of 10 minute (A), 30 minute (B), and 50 minute (C) growths. As the time of the growth increases, the size of the flakes increases. Scale bar is 50 microns.

Figure 25 also shows the size of graphene as a function of time, but with less dense samples. Every growth was performed at Torr-level pressure with 10 SCCM of argon, hydrogen, and methane. These pictures were taken of the bottom of the copper foil because the bottom is less dense. Figure 25A had a growth time of 50 minutes, Figure 25B had a growth time of 2 hours, Figure 25C had a growth time of 3 hours, and Figure 25D had a growth time of 4 hours. As the growth time increases, the size of the flakes increases.

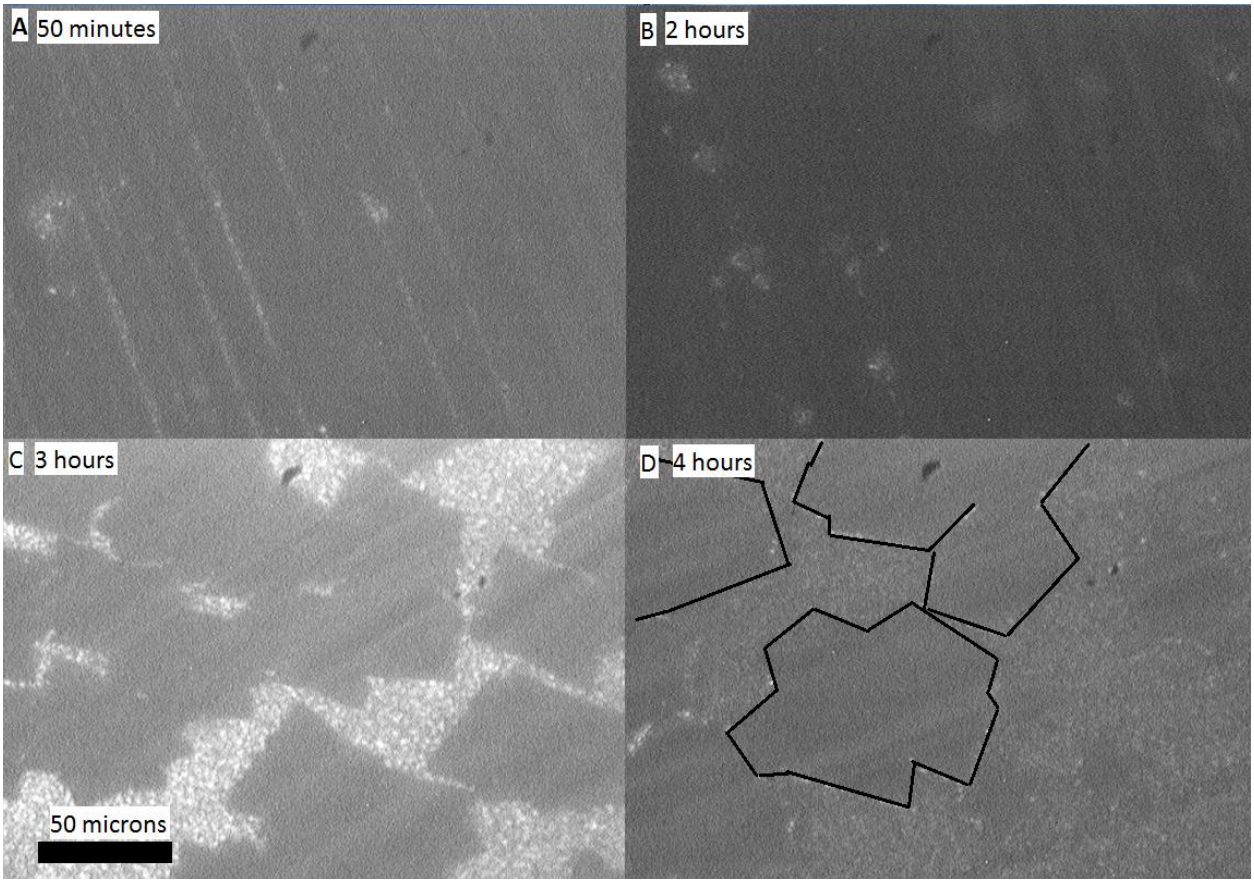


FIG. 25 Optical microscope image of 50 minute (A), 2 hour (B), 3 hour (C) and 4 hour (D) growths. Scale bar is 50 microns.

Eventually, the flakes once again will grow into other flakes. However, this long growth time shows that the copper is not evaporating away and limiting the flake size as previously discussed.

Another parameter is the flow rates of each gas. Methane is used as the source of carbon, argon as an inert gas to vary the pressure, and hydrogen to measure the effects of partial pressure of hydrogen to carbon. In Figure 26, the results of three growths are displayed. Each growth was grown for two hours, with 10 SCCM of hydrogen. The growth on the left was at the lowest pressure, with no argon and one SCCM of methane. The middle growth had 10 SCCM of argon with 5 SCCM of methane, and the growth on the right had 20 SCCM of argon with 5 SCCM of methane. As the amount of argon increased, the density of the flakes increased. Because argon is an inert gas, increasing argon should only affect the pressure, and therefore indicating that there is a direct correlation between pressure and density of flakes. As can be seen from figure 26, the size of the flakes do not increase, so the

size of the flakes is independent of pressure.

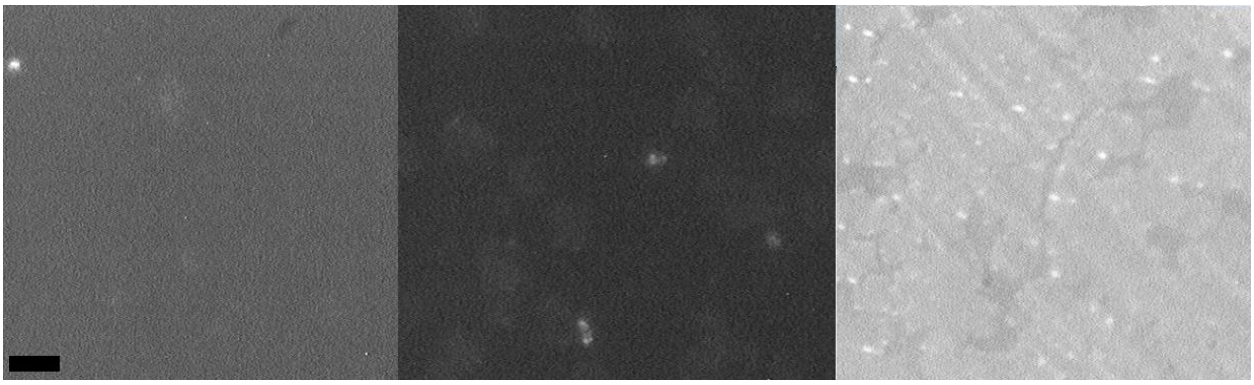

FIG. 26 Optical microscope image of growths with different flow rates of argon. Left photo had no argon flowing, the middle photo had 10 SCCM of agron, and the right photo had 20 SCCM of argon. Scale bar is 10 microns.

One of the most influential parameters within each growth was the side of the graphene foil looked at. As the copper foil sits inside of the glass tube, the top side generally was significantly more dense than the bottom side that was resting against the glass tube. An example of this occurred with a growth where we flowed 200 SCCM of Argon, 5 SCCM of Hydrogen and 10 SCCM of Methane for 30 minutes. Figure 27 shows the top of the copper foil on the left and the bottom of the copper foil on the right. The length scale is 10 microns.

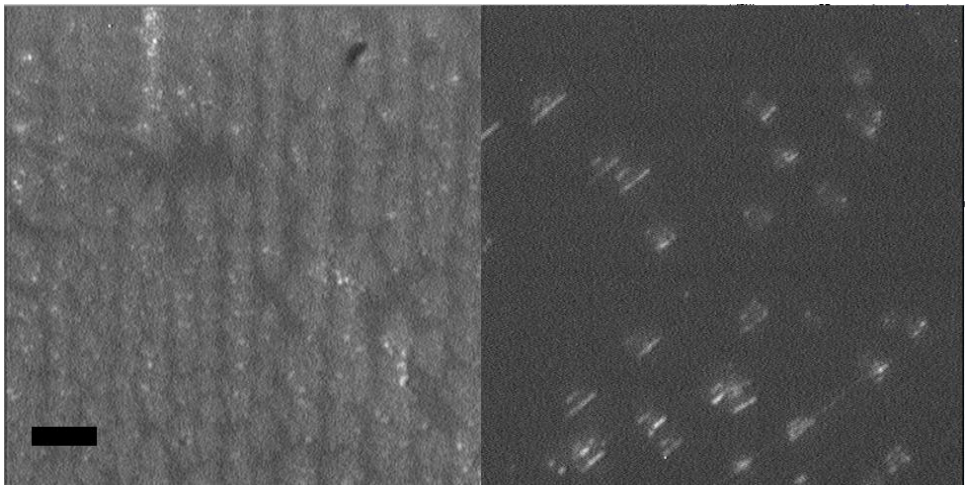

FIG. 27 Optical microscope image of the top (left) and bottom (right) surface of the copper foil during a growth. Notice the density of flakes on the top is greater than the density on bottom. Scale bar is 10 microns. (200 sccm Argon, 5 sccm Hydrogen, 10 sccm Methane for 30 minutes).

The top of the copper foil will have more air flowing over it, as it is exposed to the interior

of the glass tube, and therefore will have more methane that can react with it. With this particular growth, the flakes on the top are the same size as the flakes on the bottom. In general, the flakes on bottom were approximately half the size of the flakes on top, as can be seen from Figure 28.

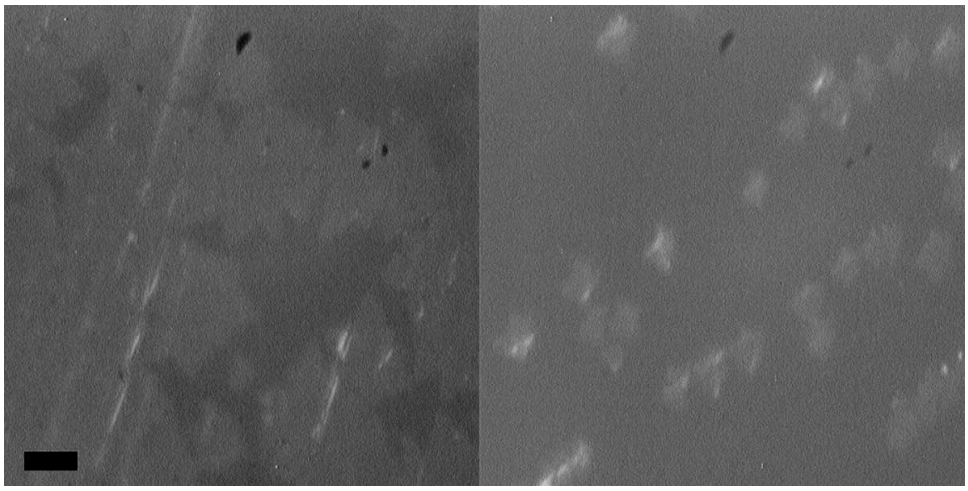

FIG. 28 Optical microscope image of the top (left) and bottom (right) of graphene growth. The flakes on bottom are about half the size of the flakes on top. Scale bar 10 microns.

However, when the flake density was too large on top, the top would grow together to form a continuous sheet, while the bottom would remain a lower density, resulting in large flakes (Figure 29).

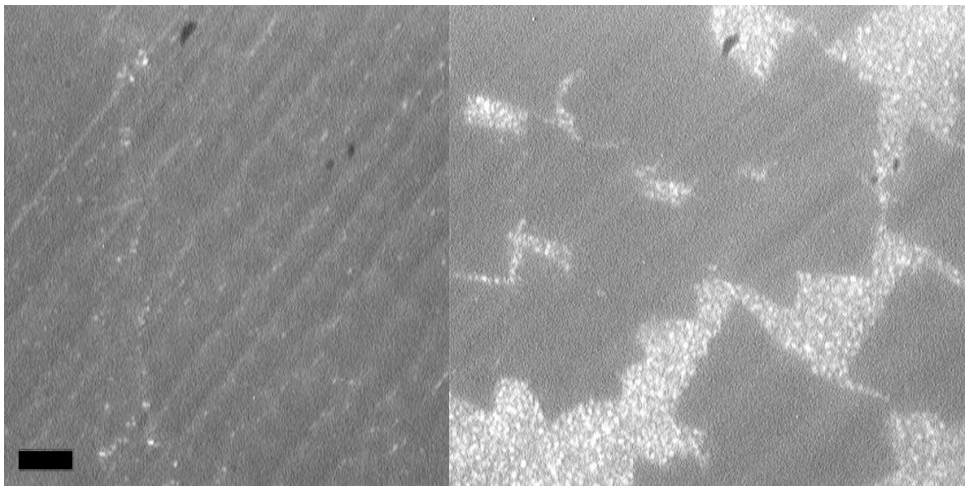

FIG. 29 Optical microscope image of the top (left) and bottom (right) of copper foil. The graphene on the top has all grown together while the graphene on bottom still has gaps between the flakes. Scale bar is 10 microns.

From these growths it is evident that the bottom of the copper foil has a lower density and smaller flakes than the top of the copper foil.

## B. Differential Reflectivity

The CVD graphene grown in the lab was then used to fabricate graphene SAMs. This section analyzes the dependency of the optical properties of a SAM on the dielectric material used in the SAM. A differential reflectivity set-up, similar to the one described in (Maas *et al.*, 2008), was used to measure the optical properties.

Graphene is transferred onto a mirror to make a graphene saturable absorber (GSA). The most common type of saturable absorber is called a Semi-Conductor Saturable Absorber Mirror (SESAM). The SESAM has made significant advances for ultrafast lasers but they still have their drawbacks. First, they are complex quantum well devices which make them expensive and difficult to fabricate. They are typically made by molecular beam epitaxy on distributed Bragg reflectors. SESAMs also are limited by their narrow bandwidth, which impacts the pulse length and versatility for lasers (Sun *et al.*, 2012).

Wide-band operation is the main characteristic that sets graphene apart from previous saturable absorbers. Due to the point-bandgap structure and linear energy dispersion of Dirac electrons, graphene saturable absorbers can operate at a wide bandwidth. In fact, GSAs have been able to produce pulses at 1, 1.25, 1.5, and 2 $\mu$m (Sun *et al.*, 2012) (Ugolotti *et al.*, 2012). GSAs boast a very fast recovery time, simple manufacturing, and a wide bandwidth.

### 1. Differential Reflectivity Set-up

*a. Description of set-up* To measure the reflectivity of a saturable absorber, a set-up similar to the reflectivity measurement set-up in (Maas *et al.*, 2008) was used (Refer to Figure 30). Within this set-up, the incoming mode-locked laser light first passes through an attenuator, which consists of two polarizers. One polarizer is on a rotational stage, and the laser light is attenuated as the polarizer transitions from parallel to perpendicular. Next, the laser light passes through an output coupler, which reflects 96.5% of the light and transmits the remaining 3.5%. The reflected light is used to measure the SAM while the transmitted

light is used as a reference beam. The (blue) reflected light passes through the chopper wheel, through a lens and is focused onto the graphene sample, where it is reflected back to the output coupler. The output coupler again reflects 96.5% of the light coming from the graphene sample, while transmitting the remaining 3.5%. The transmitted light from the graphene sample (which is $96.5\% * 3.5\% = 3.38\%$ of incoming light) is then detected by the photo detector. The reference beam (green), which is bounced off two high reflective (HR) mirrors, is also passed through the chopper wheel, and is recombined with the sample light to be detected by the photo detector. The photo detector is then passed through an Analog to Digital Converter (ADC), and finally to the CPU.

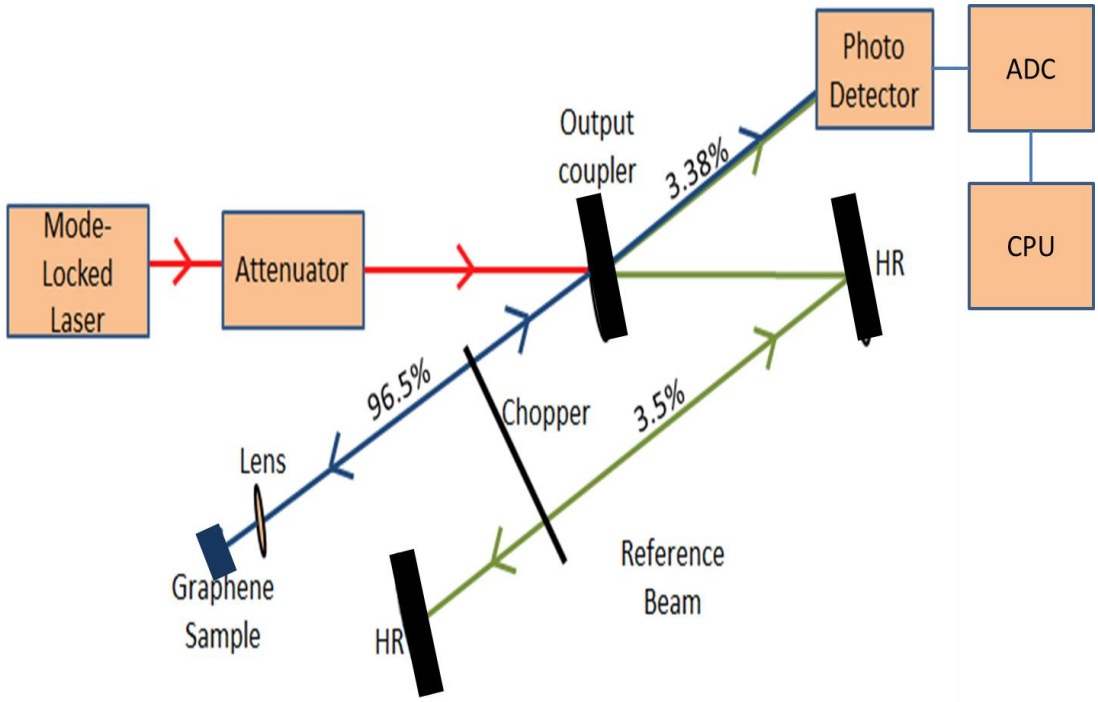


FIG. 30 Reflectivity setup. The mode-locked laser (red) first passes through the attenuator. Then, the output coupler reflects most light (blue) through the chopper and the lens and onto the graphene saturable absorber, which is reflected back through the output coupler and detected by the photo detector. The reference beam (green) is reflected using two high reflective mirrors through the copper beam, and is recombined with the sample beam (blue) to be detected by the photo detector. The photo detector is then passed through an Analog to Digital Converter (ADC), and finally to the CPU.

This set-up is superior to other set-ups because recombining the light that is reflected

from the graphene sample with the light from the reference beam enables one photo detector to detect two beams of light, which eliminates systematic error of detecting the two beams with two photo detectors.

The chopper wheel, shown in the right hand corner of Figure 31, allows for the measurement of two beams independently. This set-up was also borrowed (Maas *et al.*, 2008). In Figure 31, the offset occurs when both the reference and the sample beams are blocked by the chopper wheel. No laser light is shined on the photo detector, so this offset comes from the offset voltage of the photo detector. Then, as the wheel rotates around, it transmits the reference beam while still blocking the sample beam. As the wheel rotates more, both beams will be transmitted (the combined area in figure 31), then it will only transmit the sample beam.

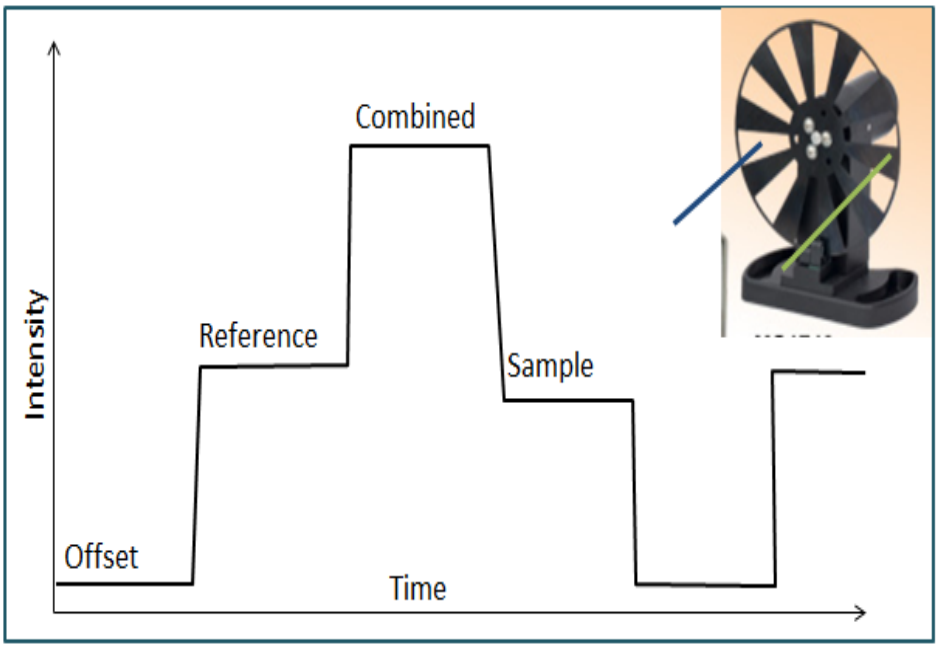


FIG. 31 The signal the photo detector receives from the chopper. When both beams are blocked by the chopper, the offset of the photo detector is the the only voltage present. Then, as the chopper wheel rotates, only the reference beam will pass through, and the reference beam is measured. The chopper wheel rotates further, both beams pass through, and finally only the sample beam passes through, allowing the measurement of the sample beam (Maas *et al.*, 2008).

Therefore, the percent reflectance can be evaluated with the equation:

$$\frac{(sample - offset)}{(reference - offset)} = \%\ transmittance$$

However, the fluence of the light has units of $\mu J/cm^2$, and the photo detector measures the intensity of the light in watts. The photo detector receives photons that are absorbed and excite electrons which then move according to an internal electric field, producing a current. The magnitude of this current is measured and outputs a value in watts. Therefore, to convert watts to determine the intensity of the light:

$$Fluence \rightarrow \frac{Pulse\ Energy}{Area} \rightarrow \frac{Average\ Power}{Repitition\ Rate * Area} \rightarrow Joules/cm^2$$

To convert fluence to intensity:

$$\frac{Fluence}{Pulse\ Duration} \rightarrow Watts/cm^2$$

*b. Data Processing* The computer code needs to determine the values of the sample, reference, offset and combined plateaus. It is structured in a way to keep the high frequency noise and eliminate the data between the transitions from one level to the next. The code maps the number of data points to each intensity, discards points that are a standard deviation away from a peak, and then takes the average intensity of each peak and assigns it to the appropriate plateau. This method is superior to taking the derivative of the data, and discarding data with a non-zero derivative, because within each plateau is high-frequency noise from the laser. This high-frequency noise is valid data, yet it has a non-zero derivative. Averaging each plateau only eliminates the data from the transition from one plateau to the next. A visual of this code is depicted in Figure 32.

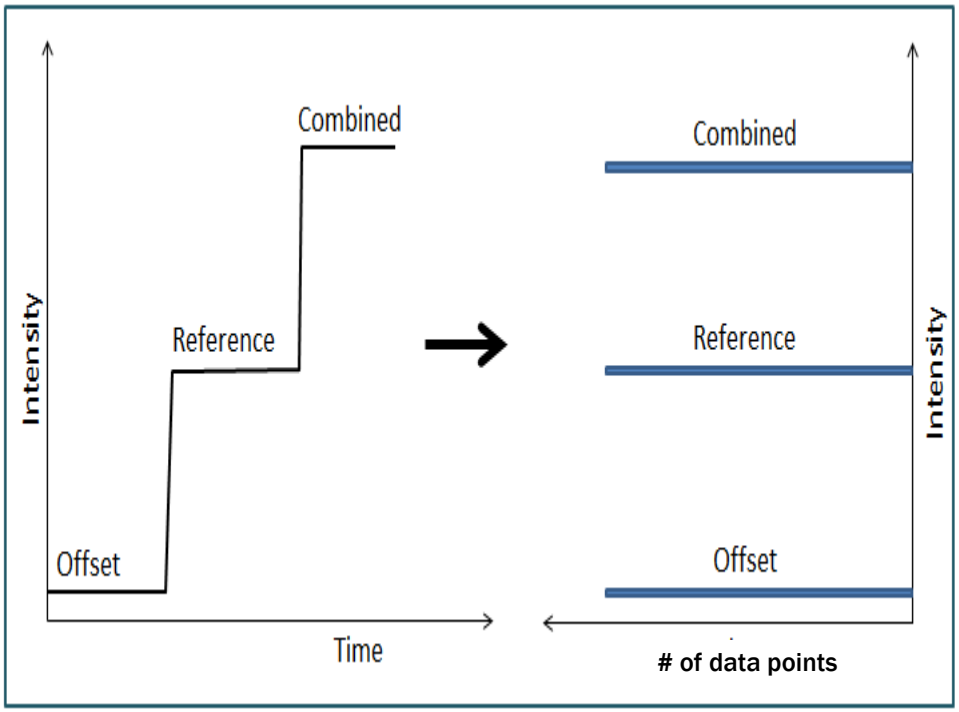


FIG. 32 Visual representation of the computer code. The code maps the number of data points to each intensity, discards points that are a standard deviation away from a peak, and then takes the average intensity of each peak and assigns it to the appropriate plateau.

### 2. Differential Reflectivity Measurements

As a sanity check, a SESAM was measured with a mode-locked laser. The laser used a Er:Yb:glass gain medium pumped by a 980nm pump laser. The output power is 16mW, with an 88MHz repetition rate, a center wavelength of 1550nm, a pulse width of 250fs, and a beam diameter of $5\mu m$. We measured the SESAM to be characterized by saturation fluence of $51 \pm 3\mu J/cm^2$, saturable loss of $0.31 \pm 0.01\%$, and non-saturable loss of $0.36 \pm 0.01\%$. These values did not quite agree with the values from the data sheet, as they were listed as saturation fluence of $70\mu J/cm^2$, saturable loss of 0.4%, and non-saturable loss of 0.6%. However, the discrepancy between the measurements and the data sheet could be due to many reasons. First, the wavelength of the laser used affects the saturation fluence and saturable loss. Second, the values on the data sheet were calculated so a factor of 2 would not be uncommon to measure. Third, each SESAM is not exactly the same, so there will be some systematic error. A 0.3% output coupler was used for the baseline measurement. The drop in reflectivity at high intensities is due to two photon absorption.

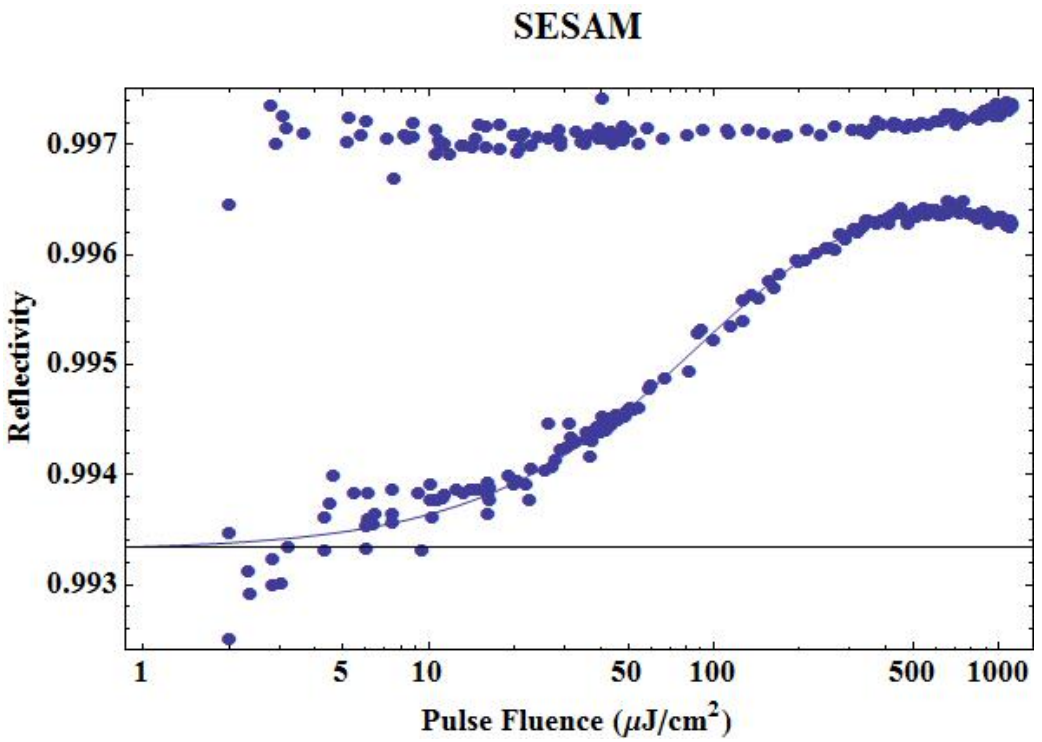


FIG. 33 SESAM differential reflectivity measurement fitted with slow saturable absorber curve. The top curve is a baseline measurement of a 0.3 % output coupler and the bottom curve is the SESAM data. Saturation Fluence $51 \pm 3 \mu Joule/cm^2$, saturable loss $0.31 \pm 0.01\%$, non-saturable loss $0.36 \pm 0.01\%$.

Notice that the baseline measurement of the output coupler is within 0.05%, which proves this set-up has a very small nonlinearity over nearly three orders of magnitude.

Graphene saturable absorbers (GSA) have a drawback: they damage before they reach the intensity regime in order to be effective at mode-locking lasers. The indicator of damage for a saturable absorber is when the absorber does not absorb as much light, so it becomes more transparent. To mode-lock a laser, the saturable absorber needs to operate above the saturation fluence to attenuate the lower intensities more. The higher above the saturation fluence that the laser operates, the more efficient the saturable aborber is. Because graphene is approximately a two-dimensional material, the dielectric that the graphene is transferred onto has a large effect on the properties of the graphene. Various dielectrics were used in graphene SAMs to determine the effect the dielectrics have on the optical properties of graphene.

The values of the alumina sample were $F_{sat} = 46 \pm 4 \mu J/cm^2$, qns $= 2.5 \pm 0.1\%$, qs $=$

$0.8 \pm 0.1\%$. The non-saturable loss was high because the alumina sample was made on a silver mirror, which has a 2% absorption. Alumina begins to damage at around $200\mu J/cm^2$. The actual absorption curve should look like the fitted curve. This damage makes a fit of an absorption curve difficult.

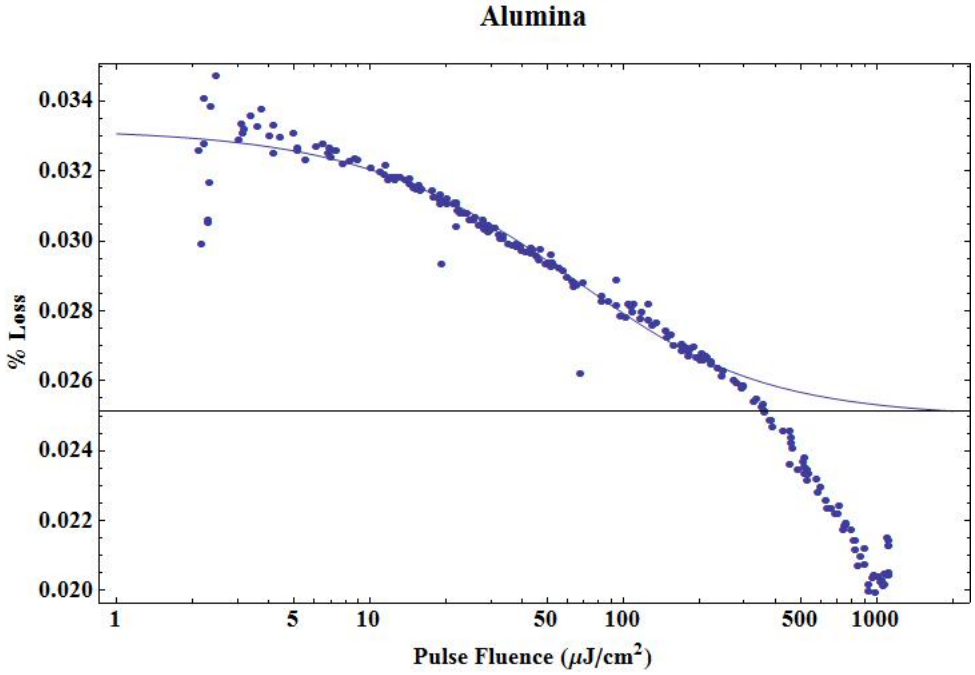


FIG. 34 SAM with an alumina dielectric fitted with an average of a slow and fast saturable absorber. The saturation fluence was $46 \pm 4\mu J/cm^2$, the non-saturable loss was $2.5 \pm 0.1\%$, and the saturable loss was $0.8 \pm 0.1\%$.

Next, we fabricated a sample using Silicon Monoxide (SiO) as the dielectric (Figure 35. Notice the points at the bottom of the curve that begin to stray off to the left. This occurred because the sample damaged at around $300\mu J/cm^2$, which caused a decrease in absorption. This damage is comparable to the Alumina sample that had a damage threshold of $200\mu J/cm^2$.

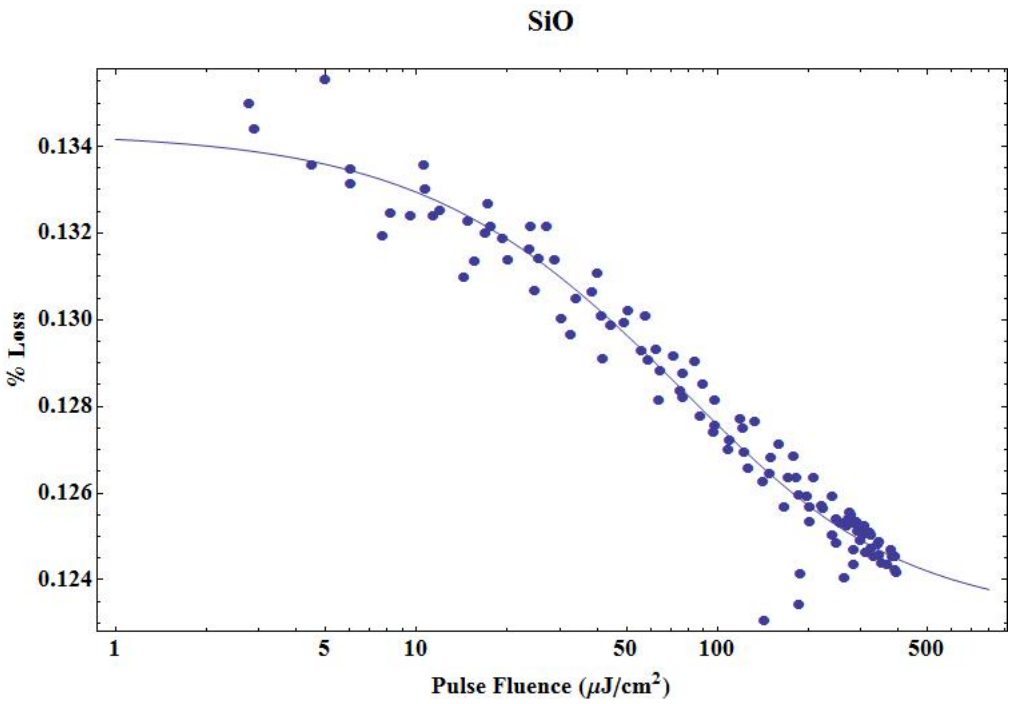


FIG. 35 This SAM was made with silicon monoxide as the dielectric. It had a saturation fluence of $54 \pm 6 \mu J/cm^2$, a non-saturable loss of $12.3 \pm 0.3\%$, and a saturable loss of $1.1 \pm 0.1\%$.

Figure 36 is the saturation curve of a $Ta_2O_5$ dielectric with bottom-coated graphene. It has a saturable loss of $2.4 \pm 0.1\%$, a non-saturable loss of $17.3 \pm 0.3\%$, and a saturation fluence of $26 \pm 2 \mu J/cm^2$. The damage threshold for the $Ta_2O_5$ was about $200 \mu J/cm^2$. Once again, the damage threshold for this saturable absorber is no better than the previous absorbers.

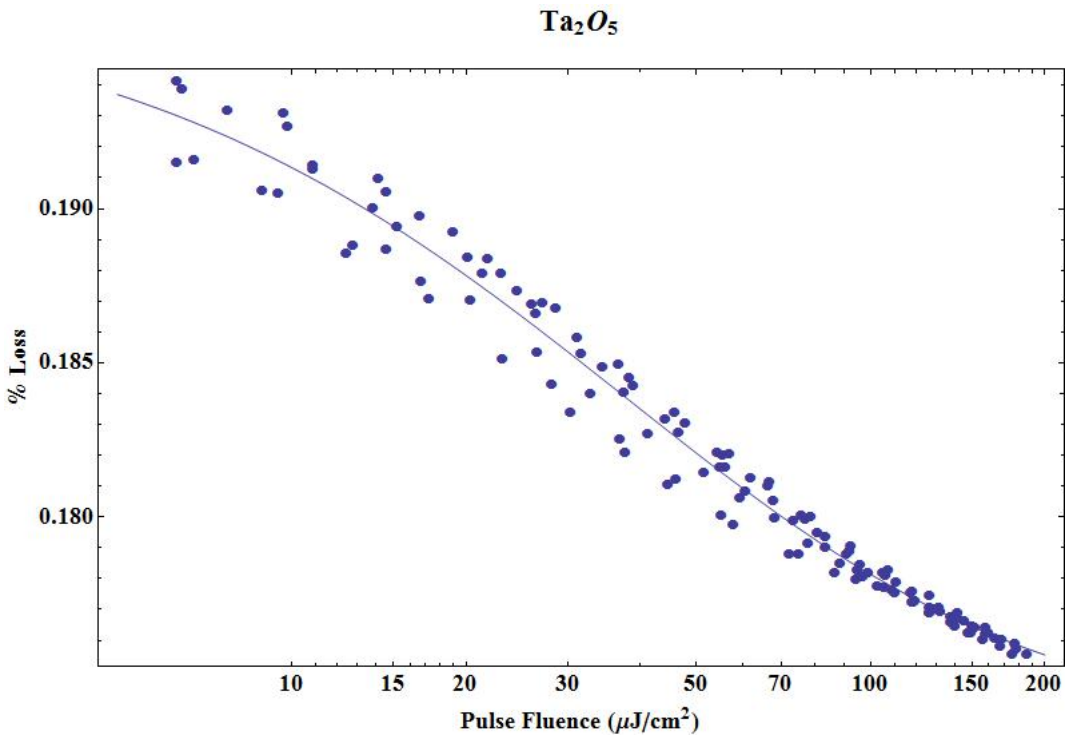


FIG. 36 SAM with a tantalum pentoxide dielectric. It showed a saturation fluence of $26 \pm 2 \mu J/cm^2$, a non-saturable loss of $17.3 \pm 0.3\%$, and a saturable loss of $2.4 \pm 0.1\%$.

Finally, in Figure 37, the saturation curve of graphene on an HR mirror is shown. This had a saturation fluence of $296 \pm 52 \mu J/cm^2$, a non-saturable loss of $2.3 \pm 0.4\%$, saturable loss of $0.56 \pm 0.04\%$ and a damage threshold of $600 \mu J/cm^2$. The field enhancement for this graphene should be about 2, so an insertion loss (qs + qns) of about four percent is expected. However, an insertion loss of around three percent was measured, which indicates the field enhancement may be slightly off.

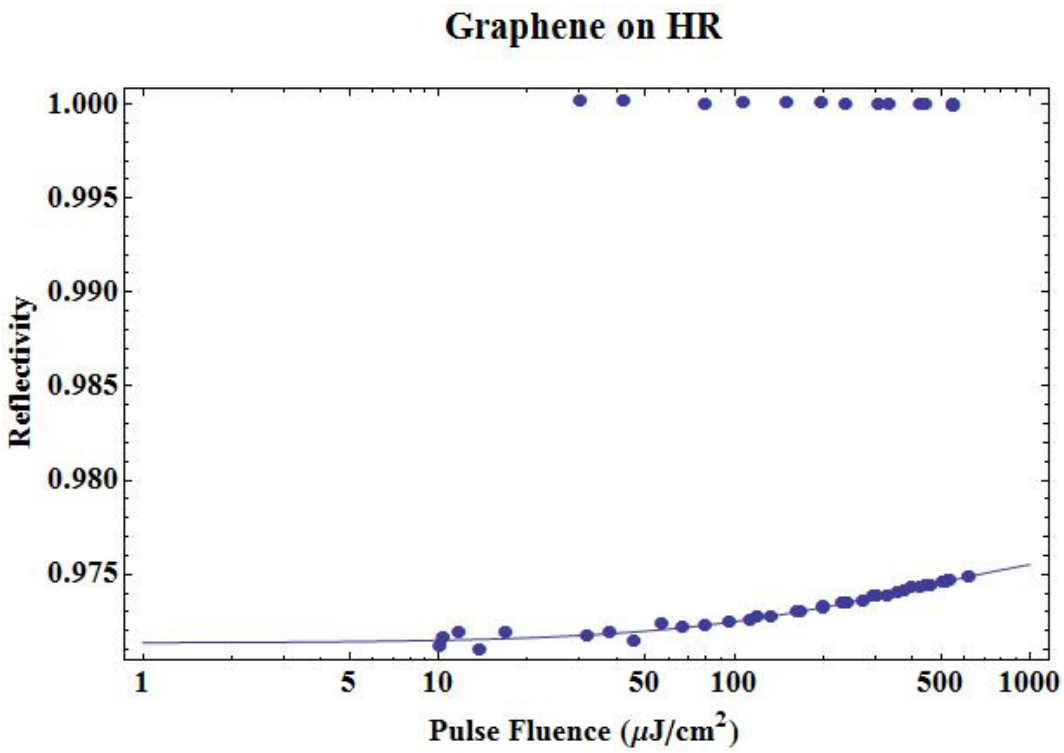


FIG. 37 This sample was made with graphene on an unknown dielectric on an HR mirror. The saturation fluence was $296 \pm 52 \mu J/cm^2$, the non-saturable loss was $2.3 \pm 0.4\%$, and the saturable loss was $0.56 \pm 0.04\%$.

In conclusion, the graphene on the HR mirror had a damage threshold of $600 \mu J/cm^2$, which is 2-3 times higher than the other samples, which had damage thresholds of $200 - 300 \mu J/cm^2$. However, the saturable to non-satuable loss of the samples demonstrate an interesting effect. For the alumina sample, qs/qns was 0.32, which is better than the graphene on HR sample of 0.24. Ideally, the larger the qs/qns ratio is, the better saturable absorber. The other samples did not have nearly as good of a ratio (SiO is 0.089 and TaO is 0.14).

### 3. Damage threshold

It is unknown what physically happens when a graphene saturable absorber damages. However, experiments were performed to investigate the damage. These experiments determined that the damage was not due to the carbon of the graphene combusting with oxygen in the air. This was determined by purging the graphene sample with Argon, as shown in Figure 38. Purging blows Argon at the sample, which blows any oxygen in the air away from

the sample. When the sample was purged, there was no effect on the damage threshold. Therefore, the damage is not due to the carbon atoms of the graphene combusting with the oxygen atoms in the air. However, the graphene may still combust with oxygen atoms that are present between the graphene and whatever substrate it is adhered to, but this cannot be determined by purging.

Another experiment was performed to investigate whether the damage is due to the high intensity of a pulsed laser or the average power of the laser. When the incoming laser light is mode-locked, the light comes in short, high intensity pulses. When the incoming light is not mode-locked, the light is continuous with low intensity, but has the same average power (shown on bottom of Figure 38). When a mode-locked laser was used the saturable absorber damages, but when a continuous wave laser was used the saturable absorber does not damage. This indicates that the damage results from the high intensity of a pulsed laser, not from the average power of the laser.

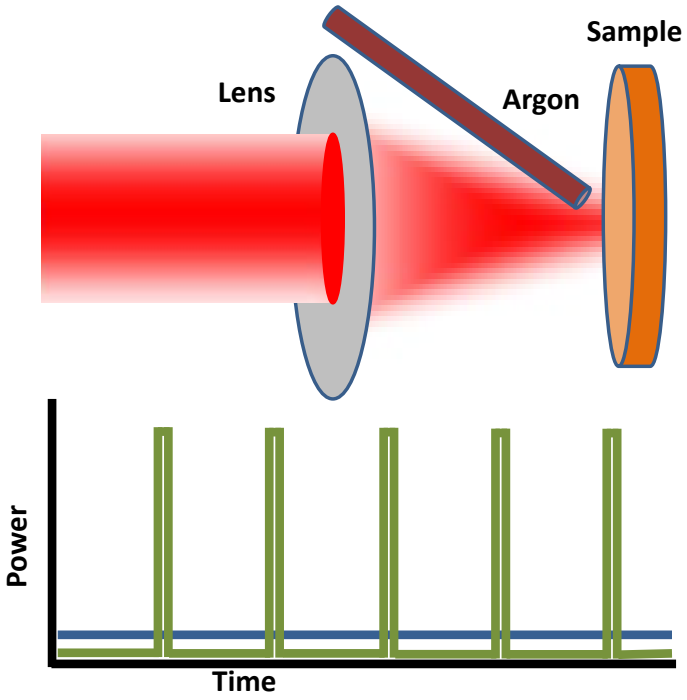


FIG. 38 Cartoon of purging a saturable absorber with Argon. Argon blows away any oxygen that may be next to the sample, which will let us know if the sample combusts with the oxygen in the air. On bottom shows the pulsed mode-locked laser (green) and the average power/continuous wave laser (blue).

## VII. CONCLUSION

Overall, my research investigated parameters of graphene CVD growth and discovered more about the limits of using graphene as a saturable absorber at $1.5\mu m$. However, graphene may be an excellent absorber at longer wavelengths because the saturation fluence is much lower and therefore can still operate at intensities below the damage intensity. Improved CVD recipes resulted in larger, higher quality graphene that can be used for saturable absorbers, mechanical membranes, transistors, polarizers, capacitors, and other electronic devices. High quality graphene is important to these devices because when the devices are fabricated with high quality graphene, it enables us to investigate the properties of pure graphene. Imperfect graphene complicates measurements because it adds an extra factor in attempting to study which results are due to the graphene and which results are due to the imperfections.

Knowledge about the limits of using graphene as a saturable absorber at $1.5\mu m$ allows us to construct graphene saturable absorbers that optimize saturable absorption. Optimal saturable absorbers are desirable because they are more efficient at mode-locking lasers, which are useful for a much more broad range of applications like ultra-precise timing and high-resolution spectroscopy.

### A. Future Directions

Given the opportunity to go further into my research, I would continue to investigate CVD recipes and test more saturable absorber samples. I would explore different substrates other than copper to grow graphene on. I have a particular interest in platinum since reading the paper (Gao *et al.*, 2012).

For differential reflectivity, I would like to measure samples with different thicknesses of dielectrics to see if the field enhancement equations are correct. I would like to further investigate alumina and graphene on HR to try to achieve better saturable absorbers. Finally, a differential reflectivity of free standing graphene while purging both sides would definitively inform us whether or not the carbon was combusting with oxygen when it damages.

## References

Carmichael, H., G. Foster, U. Keller, and A. Maradudin, 2004, *Progress in Optics*, volume 46 (Elsevier, Amsterdam).

Castro Neto, A. H., F. Guinea, N. M. R. Peres, K. S. Novoselov, and A. K. Geim, 2009, Rev. Mod. Phys. **81**, 109, URL http://link.aps.org/doi/10.1103/RevModPhys.81.109.

Gao, L., W. Ren, H. Xu, J. Li, and Z. Wang, 2012, Nat Commun. **3**(3), ISSN 699, URL http://www.ncbi.nlm.nih.gov/pmc/articles/PMC3293422/.

Geim, A. K., and K. S. Novoselov, 2007, Nat Mater **6**(3), 183, ISSN 1476-1122, URL http://dx.doi.org/10.1038/nmat1849.

Huang, P. Y., C. S. Ruiz-Vargas, A. M. van der Zande, W. S. Whitney, M. P. Levendorf, J. W. Kevek, S. Garg, J. S. Alden, C. J. Hustedt, Y. Zhu, J. Park, P. L. McEuen, *et al.*, 2011, Nature **469**(7330), 389, ISSN 0028-0836, URL http://dx.doi.org/10.1038/nature09718.

Kim, R., V. Perebeinos, and P. Avouris, 2011, Phys. Rev. B **84**, 075449, URL http://link.aps.org/doi/10.1103/PhysRevB.84.075449.

Lee, C.-C., J. Miller, and T. Schibli, 2012a, Applied Physics B **108**, 129, ISSN 0946-2171, URL http://dx.doi.org/10.1007/s00340-012-5095-5.

Lee, C.-C., S. Suzuki, W. Xie, and T. R. Schibli, 2012b, Opt. Express **20**(5), 5264, URL http://www.opticsexpress.org/abstract.cfm?URI=oe-20-5-5264.

Li, H., Y. Anugrah, S. J. Koester, and M. Li, 2012, Applied Physics Letters **101**(11), 111110 (pages 5), URL http://link.aip.org/link/?APL/101/111110/1.

Li, Z., P. Wu, C. Wang, F. Xiaodong, W. Zhang, X. Zhai, C. Zeng, Z. Li, J. Yang, and J. Hou, 2011, ACS Nano **5**, 3385, ISSN 4, URL http://pubs.acs.org/doi/abs/10.1021/nn200854p.

Liu, M., X. Yin, and X. Zhang, 2012, Nano Letters **12**(3), 1482, URL http://pubs.acs.org/doi/abs/10.1021/nl204202k.

Maas, D. J., B. Rudin, A.-R. Bellancourt, D. Iwaniuk, S. V. Marchese, and U. Keller, 2008, Opt. Express **16**(10), 7571, URL http://www.opticsexpress.org/abstract.cfm?URI=oe-16-10-7571.

Nagai, H., M. Nakano, K. Yoneda, H. Fukui, T. Minami, S. Bonness, R. Kishi, H. Takahashi, T. Kubo, K. Kamada, K. Ohta, B. Champagne, *et al.*, 2009, Chemical Physics Letters **477**(46), 355 , ISSN 0009-2614, URL http://www.sciencedirect.com/science/article/pii/

S0009261409008562.

Sun, Z., T. Hasan, and A. Ferrari, 2012, Physica E: Low-dimensional Systems and Nanostructures **44**(6), 1082 , ISSN 1386-9477, URL http://www.sciencedirect.com/science/article/pii/S1386947712000252.

Sun, Z., Z. Yan, J. Yao, E. Beitler, Y. Zhu, and J. M. Tour, 2010, Nature **468**(7323), 549, ISSN 0028-0836, URL http://dx.doi.org/10.1038/nature09579.

Svelto, O., 1989, Principles of Lasers Third Edition, 3.

Ugolotti, E., A. Schmidt, V. Petrov, J. W. Kim, D.-I. Yeom, F. Rotermund, S. Bae, B. H. Hong, A. Agnesi, C. Fiebig, G. Erbert, X. Mateos, *et al.*, 2012, Applied Physics Letters **101**(16), 161112 (pages 4), URL http://link.aip.org/link/?APL/101/161112/1.

Wei, D., Y. Liu, Y. Wang, H. Zhang, L. Huang, and G. Yu, 2009, Nano Letters **9**(5), 1752, pMID: 19326921, URL http://pubs.acs.org/doi/abs/10.1021/nl803279t.

Widom, B., 2002, Cambridge University Press ISSN 9780521811194, URL http://assets.cambridge.org/97805218/11194/excerpt/9780521811194_excerpt.pdf.

Wood, J. D., S. W. Schmucker, A. S. Lyons, E. Pop, and J. W. Lyding, 2011, Nano Letters **11**(11), 4547, URL http://pubs.acs.org/doi/abs/10.1021/nl201566c.

Zhang, B., W. H. Lee, R. Piner, I. Kholmanov, Y. Wu, H. Li, H. Ji, and R. Ruoff, 2012, ACS Nano **6**, 2471, ISSN 3, URL http://pubs.acs.org/doi/full/10.1021/nn204827h.